University of Leoben

Oxidation Behavior of Ti-Al-Si-N and Ti-Al-B-N Coatings

Diploma Thesis

by

Johannes Zechner

Leoben, June 2008

This work has been carried out in cooperation with CERATIZIT Austria G.m.b.H., CERATIZIT Luxembourg S.à.r.l. and Materials Center Leoben Forschung G.m.b.H., at the Department of Physical Metallurgy and Materials Testing, University of Leoben.

Affidavit

I declare in lieu of oath, that I wrote this thesis and performed the associated research myself, using only literature cited in this volume.

Leoben, June 2008

(Johannes Zechner)

Acknowledgements

I would like to thank O.Univ.-Prof. DI. Dr. Helmut Clemens, Head of the Department of Physical Metallurgy and Materials Testing, for giving me the opportunity to carry out this work at his institute.

I am very grateful to Ao.Univ.-Prof. DI Dr. Reinhold Ebner, Managing Director of the Materials Center Leoben, for giving me the opportunity to write this thesis within a MCL project.

My sincerest gratitude and appreciation are due to Ao.Univ.-Prof. DI Dr. Christian Mitterer, Head of the Thin Films Group at the Department of Physical Metallurgy and Materials Testing, for his kindness, expertise and the supervision of this thesis.

Special thanks go to my supervisor DI Martin Pfeiler, for assigning me this work, his patience, support and the countless valuable discussions.

Furthermore I want to express my gratitude to DI Dr. Martin Kathrein, at CERATIZIT Austria G.m.b.H., DI Claude Michotte, at CERATIZIT Luxembourg S.à.r.l., and the respective companies for their excellent support of this work.

I am very thankful to all members of the Department of Physical Metallurgy and Materials Testing and especially my colleagues and friends at the Thin Films Group. Special thanks go to Priv.-Doz. DI Dr. Paul Mayrhofer, for performing the TEM measurements and his help with data evaluation and interpretation.

1 Introduction

Materials used in machining applications, e.g. tool steels or cemented carbides, are subjected to conditions such as high wear and temperatures, mechanical loads and corrosive environments. Being the junction to the environment, the tool surface thus has to fulfill the highest demands on material resistance in the respective application. Coating the tool gives the possibility to combine the beneficial properties of the bulk and the coating material, resulting in a composite posessing properties, which could not be provided by a single monolithic material. The bulk material provides strength and stiffness for the tool, while the coating protects it from wear and corrosive damage.

Most tools used for cutting applications nowadays are coated by either physical vapor deposition (PVD) or chemical vapor deposition (CVD) before being applied. The first coating successfully used in industry for the machining of steel was TiN, considerably improving both the lifetime of the tools and the working conditions like cutting speed and feed rate. The continuously growing demand of the cutting industry for higher cutting speeds and feed rates, led to the development of coatings based on TiN with further incorporated elements like Al or C. The most important representative of these is $Ti_{1-x}Al_xN$, which is characterized by improved wear and oxidation resistance compared to TiN. The temperature where an onset of oxidation can be observed is shifted from 550 °C for TiN to about 700°C for the Al containing $Ti_{1-x}Al_xN$ [1].

Due to economical interests and reasons of environmental protection, the cutting industry is interested in a reduction of lubricants and coolants with the long term goal of a complete abandonment of these additives and resulting dry cutting. Intensive research work is needed to comply with these demands of lubricant and coolant reduction in machining applications, which lead to a further increase in the occuring temperatures. Scientific research has focused on the development of new, and an enhancement of already existent, material combinations, with respect to oxidation and self lubrication [2].

Against this background of continuously rising temperatures and the increasing danger of tool failure due to coating oxidation, the conducted work has the goal to examine the influence of different alloying elements and an increased bias voltage (V_B) during deposition on $Ti_{1-x}Al_xN$ coatings. Si and B were chosen as elements which should be alloyed into a standard $Ti_{1-x}Al_xN$ coating. Vaz et al. [3] already tested a similar coating composition alloyed with high (~10 at.%) Si contents and found an improvement of both mechanical and oxidation properties. Also coatings alloyed with

B were already investigated, e.g. by Rebholz et al. in [4], who found good mechanical performance for these coatings. In the present work the alloying element contents are chosen rather low with 0.5 and 2 at.% for Si and 0.1 and 0.5 at.% for B. Additionally the influence of different values of V_B on the oxidation behavior of the unalloyed and alloyed coatings is observed. The V_B values were chosen between -40 V and -160 V and were applied to all coating compositions tested [3, 4].

As a result of the chosen industry-based approach the examined coatings are produced in an industrial scale coating plant and provided by Ceratizit Luxembourg. They are oxidized for different times at various temperatures to obtain an overview on the onset and progress of oxidation of the different coatings. The investigations concentrate on the examination of the coating composition and structure of both the as-deposited as well as the oxidized coatings. Furthermore oxide layer thickness and structural properties of the oxide layer shall be investigated.

2 Theoretical Background

2.1 PVD Techniques

2.1.1 General

PVD is a nowadays widely used method of depositing thin films for a large number of applications, ranging from decorative films to hard coatings for tool protection. The success of PVD is based on the wide variety of possible combinations of coatable materials and coatings. Starting in the second half of the 20th century a variety of techniques has been developed, which can be divided into two basic groups based on high-vacuum technology. The main process variants, sputtering and evaporation (Fig. 2.1a, b), differ in the mechanisms the condensed feed material, called target, is vaporized [2, 5].

Sputtering is characterized by the vaporization of the solid coating material by high energetic inert gas ions, e.g. Ar. The energetic ions are provided by a plasma burning between the target cathode and the walls of the high vacuum chamber. In DC sputtering a voltage of -1 to -5 kV is applied, which ignites a glow discharge on introduction of an inert gas. The ions are accelerated towards the target and on impact, they interact with the target material resulting in the emission of X-rays, secondary electrons and if the energy is high enough also atoms of the material. Thus a wide variety of enhancements of this process is in use involving radio frequency sputtering (RF sputtering) and the use of permanent magnets behind the cathodes, called magnetron sputtering. Sputtered coatings show good adhesion but coating thickness is relatively irregular and the deposition rates are rather low [1, 2, 5, 6].

In **evaporation** processes the transition from the condensed matter to the vapor phase is accomplished by the input of thermal energy via different methods. The material can either be resistance or induction heated in a crucible, or the energy is provided by an electron or laser beam, which melts and vaporizes the source, resulting in a vapor phase consisting mostly of neutral particles and a very small fraction of ions. Due to the high vacuum conditions (10^{-3} to 10^{-6} Pa), the mean free path of the particles is long compared to the source to substrate distance and collision free line of sight transport can be assumed, leading to vapor condensation directly above the source. Limiting factors of the above mentioned techniques are the often existing pool of melted coating material and the linear line of sight transport trajectory. These factors constrain the possibilities of deposition, to vertical down-up arrangements of source and substrate.

Advantages of evaporation compared to sputtering are the higher possible deposition rates combined with satisfactory adhesion and a more evenly distributed coating thickness [1. 2, 5].

A disadvantage of evaporation is the rather low energy (~2 eV), compared to sputtering where energies of 10-100 eV can be reached. The higher kinetic energy of the arriving atoms has proven to be beneficial for the coating properties. This led to the development of **ion plating** (Fig. 2.1c), where the evaporated atoms are partly ionized by a plasma. Furthermore, the substrate is on negative potential, which accelerates the ions towards the substrate, causing a constant bombardment of the substrate and the growing film. This results in improved adhesion, microstructure and deposition rate, while at the same time the substrate temperature is kept rather low (T_S<300 °C).

The mentioned processes are not limited to the deposition of the material provided by the target. By using reactive gases like nitrogen or acetylene also nitrides and carbides can be deposited.

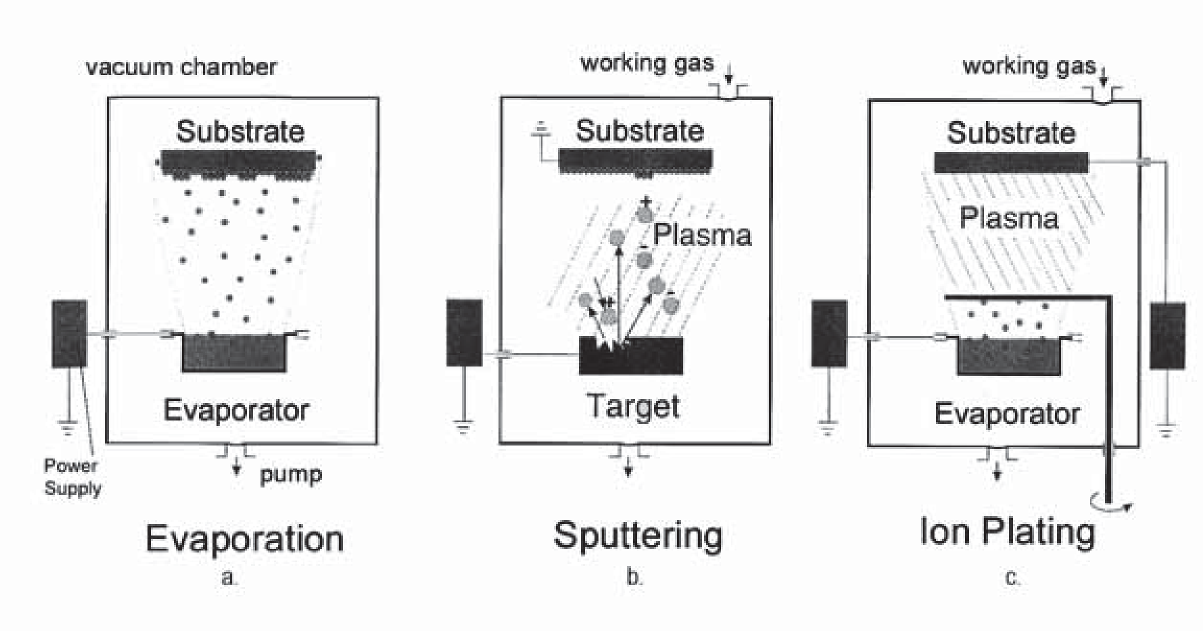

Fig. 2.1 Schematic drawing of the basic PVD and ion plating processes [5].

2.1.2 Cathodic Arc Evaporation

Cathodic arc evaporation (CAE) is an ion plating technique based on the evaporation of the target by a vacuum arc. Beginning with the patents of Snaper and Sablev in 1971 and 1974 respectivley, CAE has become one of the mostly used large scale industrial deposition methods for wear resistant coatings [5].

Features of CAE are:

- Nearly full ionization of the vapor phase.

- The plasma contains multiply charged ions.
- The high ion energies between 20 eV for light and 200 eV for heavy elements.

These characteristics give rise to certain beneficial effects on the coating properties as listed in [6]:

- High film adhesion and density.
- High deposition rates with excellent coating uniformity.
- High quality, stoichiometric reacted coatings over a wide range of processing conditions.
- Low substrate temperatures during deposition.

The CAE Process

In CAE an arc is ignited on the surface of the cathodic target, in an arc discharge circuit with the anodic recipient. Rother et al. [11] use the term vacuum arc for a self sustaining discharge burning in gases and vapors at pressures below 10^3 Pa, exhibiting high currents of around 100 A and low voltages of several 10 V. The vapor, consisting of ions and neutrals, is needed for current conduction within the gap between cathode and anode [5, 6, 8, 9, 11].

On the cathode surface the arc is concentrated on a very small area called the cathodic arc spot. In this spot, with a diameter of approximately 10^{-8} to 10^{-4} m, an extremely high current density of order 10^{12} A/m² is concentrated. The high current density in turn is associated with a high areal power density of about 10^{13} W/m², which provides sufficient energy for the phase transformation of the solid cathode material to a nearly completely ionized plasma. The explosion like evaporation produces a vapor phase consisting mainly of single or multiple charged ions, and small fractions of neutrals. Where the energetic input is not sufficient to cause direct evaporation, the target material melts and liquid macroparticles are ejected from the cathode. When built into the deposited coating they are called droplets and represent mechanically weak spots, which makes their avoidance an important issue in CAE [5, 2, 6, 7, 8, 9].

Fig. 2.2a shows the events taking place in the cathodic arc spot. The arc spot is formed at a peak of the cathodes surface roughness due to the high field electron emission there. This leads to rapid heating of the peak until it evaporates and a crater is formed, which grows with time due to joule heating. Inside the crater, the high temperature of the vapor leads to high pressures of up to 200 bar, causing the ejection of the plasma into the chamber space, giving the so called plasma jet. The ions are accelerated nearly perpendicularly away from the target with high speeds, corresponding to the high energies mentioned above. The crater grows until a critical size is reached and the power density becomes insufficient to maintain the arc which then exstinguishes. During the lifetime of one arc spot (5-40 ns), a new surface tip is formed at the crater edge, which acts as starting point for a new arc spot. In this way, the arc randomly moves over the cathode surface with a velocity of about 100 m/s. The track formed by the arc is shown in Fig. 2.2b [5, 2, 6, 7, 8, 9, 10, 11].

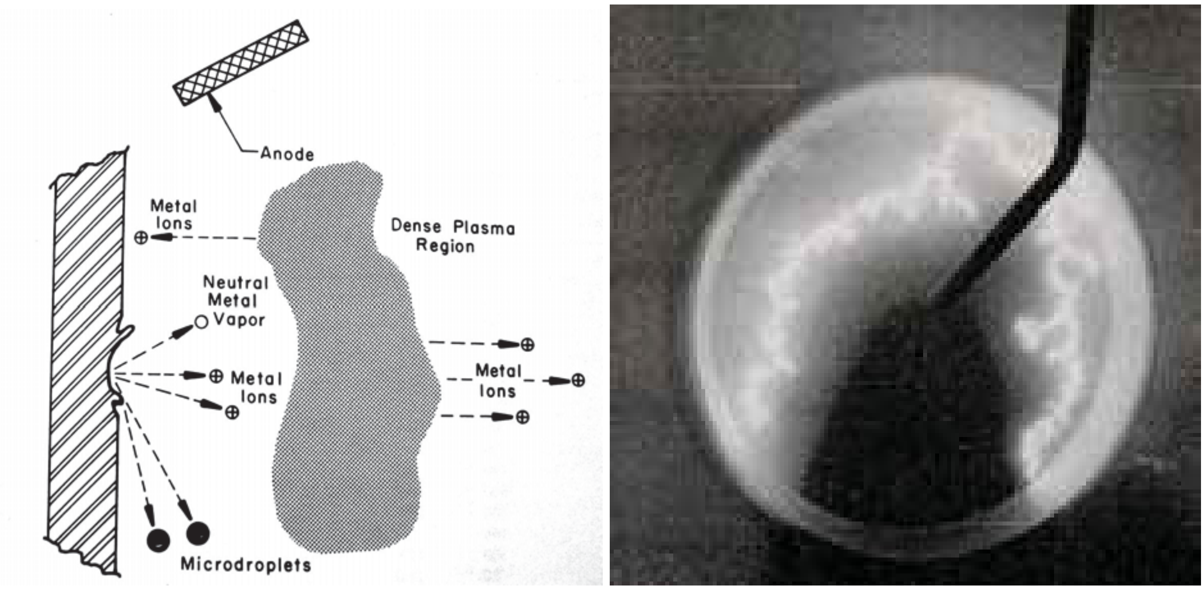

a) b)

Fig. 2.2 (a)Cathode spot region of a vacuum arc [6]. (b) Random arc discharge track on a Ti cathode [10].

Practical Aspects of CAE

CAE deposition systems normally consist of a vacuum chamber with the cathodic arc sources and a substrate fixture placed inside. A sketch of a cathodic arc source is drawn in Fig. 2.3. Besides the already described cathode and anode, a mechanical igniter is shown which is used to ignite the arc. In most cases it is a contactor touching the cathode for a short moment and spikes the arc via contact ignition. Alternatively rf ignition or so called gas igniters may be used, which have the advantage of being contact-free [6, 10, 11].

In principle, there are two possible operational modes for the application of CAE systems, pulsed and continuous. In the pulsed mode the arc is repeatedly extinguished and ignited, giving the cathode time to cool between the pulses. This technique has the disadvantage of lower deposition rates compared to the continous mode, but fewer droplets are emitted. As mentioned above, the arc moves randomly over the cathode surface and every surface that is on cathode potential. The random arc thus might leave the cathode and get extinguished. Furthermore a random arc might get concentrated at certain points on the cathode which leads to inhomogeneous target utilization and increased droplet formation. Several methods are in use to confine the arc to the cathode surface and reduce droplet emission. Sablev invented a boundary shielding exstinguishing the arc when leaving the cathode. Also permanent magnets or magnetic coils (see Fig. 2.3) can be used to control the path of the arc, which is then called a steered arc [5, 2, 6, 11].

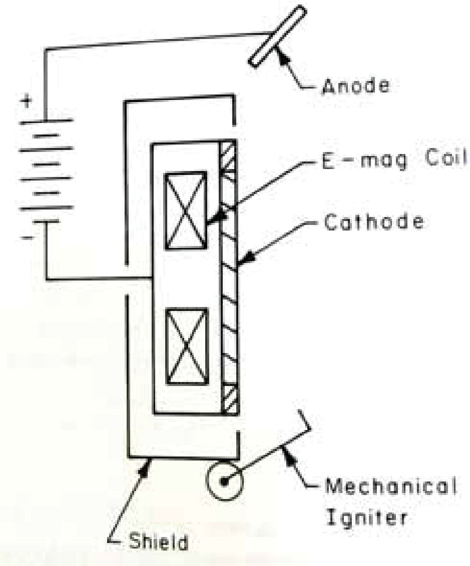

Fig. 2.3 Cross-sectional view of a cathodic arc source [6].

Droplets and their Avoidance

Droplets are reported to have a size of 0.1-10 µm, although the lower boundary is only the limit of detection and probably not the actual smallest droplet size. Size and number of occuring droplets are dependent on the melting point of the target material, the arc current, the cathode temperature, applied magnetic fields, gas species and their pressure. Fig. 2.4a shows two droplets incorporated in the coating increasing the surface roughness and decreasing mechanical properties due to the less dense structures and the weaker bonding between droplet and coating. There are several possible ways to inhibit the presence of droplets in the coatings.

Droplets are emitted at rather low angles, while the plasma is ejected nearly perpendicular to the surface as can be seen in Fig. 2.2a. This makes it possible to introduce a low angle shielding near the cathode preventing the droplets to reach the substrate. Also different forms of macroparticle filters have been introduced, working with electrostatic or magnetic plasma optical systems, separating the plasma and the macroparticles. The most commonly used arrangement was introduced by Aksenov and is shown schematically in Fig. 2.4b. It consists of a curved metal tube and a magnetic field parallel to the walls of this quarter torus. It has proven to succesfully separate the ions, which are following the magnetic field, and the neutrals and droplets, who are collected inside the tube. Various other forms of filters have been developed, which were reviewed by Karpov [12]. They all lead to nearly macroparticle free coatings with enhanced properties over coatings deposited without filters. Limiting to the use of these filters are the industrial disadvantages of increasing the complexity of the deposition plants as well as lowering the deposition rates, which lead to increased process times and higher costs [6, 7, 10, 11, 12, 13, 14].

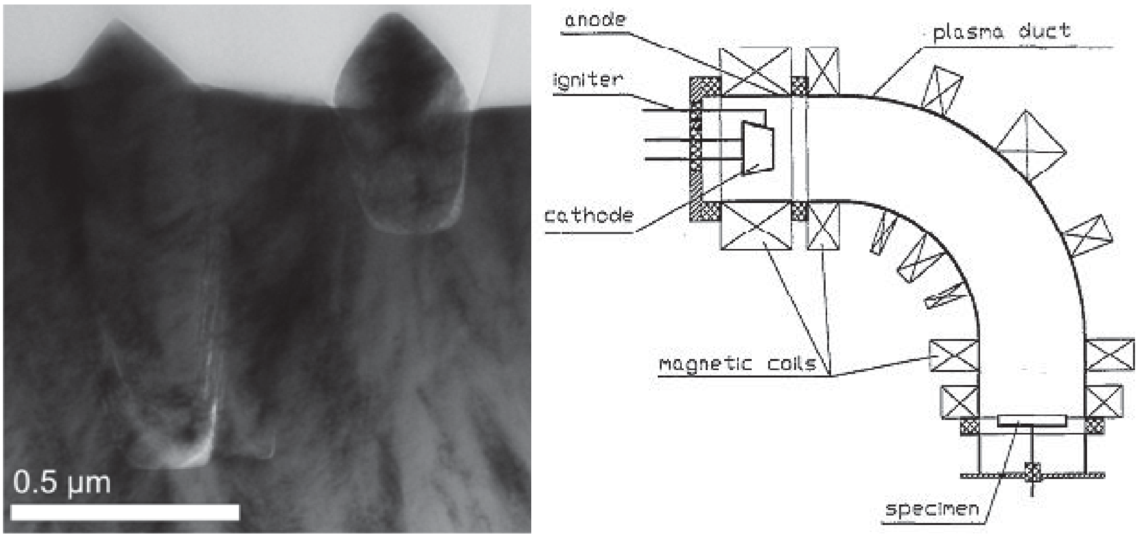

a) b)

Fig. 2.4 (a) TEM image of two droplets. (b) Aksenov macroparticle filter design [12].

2.2 Nucleation and Growth of Thin Films

The coating properties are primarily influenced by the way the coating grows, which itself is influenced by parameters like the coating technique, working pressure, substrate temperature and bias voltage. Thus the properties of materials deposited as thin films can not be compared to the bulk materials due to the different microstructure, e.g. the smaller grain size, columnar growth, metastable phases and different defect structure.

An atom hitting the substrate can be directly reflected, or it transfers sufficient amounts of energy to be loosely adsorbed, becoming an ad-atom moving over the surface or being desorbed again. The ad-atoms not desorbed can form clusters of, first subcritical and on arrival of more atoms, critical size, called nuclei. After a nucleus is formed, it starts to grow in one of three distinguishable modes shown in Fig. 2.5. The first mode, called island (or Volmer-Weber) growth, is observed when the deposited atoms are bound stronger to each other than to the substrate. Layer, or Frank-Van der Merwe, growth occurs in the opposite situation when the binding between substrate and coating atoms is stronger than between the coating atoms themselves. The third possible growth mode is a combination of layer and island growth and is called Stranski-Krastanov mode. It appears when at first monolayers are formed but with growing distance from the substrate, island growth becomes more favourable. All three modes are found in different combinations of substrate and coating materials [8, 11, 17].

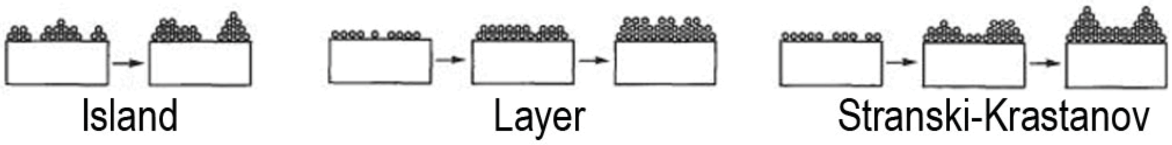

Fig. 2.5 The three basic modes of early thin film growth [8].

Further growth of the nuclei and crystals is influenced by four basic processes, namely shadowing, surface diffusion, bulk diffusion and desorption. Shadowing (angle-of-incidence effect) is a geometrical effect, caused by the substrates surface roughness and the line-of-sight transport of the vapor species, which prevents a homogeneous supply of atoms for every position on the substrate. The three other mechanisms are dependent on their activation energies and can therefore be scaled with the melting temperature (T_m) of the deposited species [8, 17].

2.2.1 Structure Zone Models

In 1969, Movchan and Demchishin (M & D) published their results on observations of evaporated thick films, where they connected structure and morphology of the coating only to the homologous temperature T_s/T_m (with T_s being the actual film temperature), as shown in Fig. 2.6a. In this first so called structure zone model (SZM) they distinguished between three zones labeled 1 ($T_s/T_m<0.3$), 2 ($0.3<T_s/T_m<0.5$) and 3 ($0.5<T_s/T_m$). Thornton extended this model for sputtering processes, introducing the argon gas pressure as another variable and a zone T, inserted in the range $0.2< T_s/T_m<0.4$, confining the neighbouring zones (see Fig. 2.6b).

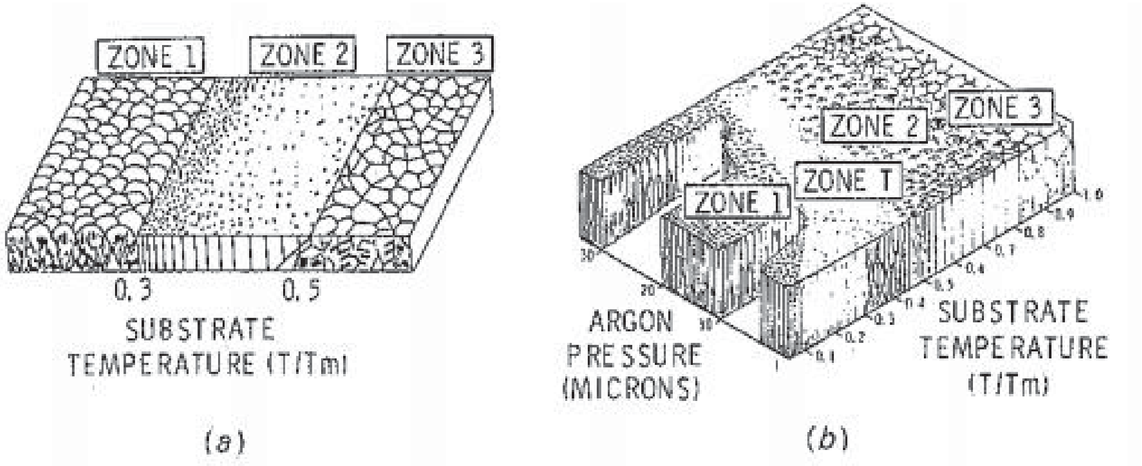

Fig. 2.6 Structure zone models for coating growth. (a) Proposed by Movchan and Demchishin. (b) Model proposed by Thornton for sputtered coatings [19].

Zone 1 microstructure consists of tapered columns, with domed tops, often pointing in the direction of the vapor flux, which are surrounded by porous boundaries. The columns are composed of smaller crystals or can be amorphous and their size increases with increasing temperature. This structure results from geometrical shadowing combined with negligible ad-atom mobility.

In the range of $0.2<T_s/T_m<0.4$ the Zone T appears as a transition between zones 1 and 2 of the M & D model. Characteristic here is the dense array of tightly packed fibrous grains, with dense grain boundaries, which do not extend over the whole coating thickness. Remarkable are the better surface morphology and higher coating density than in the two adjacent zones. Responsible for this structure is the considerable surface diffusion, which is able to balance the inhomogeneous supply of arriving atoms, caused by shadowing effects, while grain boundary motion in this temperature interval is still constrained.

Both surface and bulk diffusion are active at even higher homologous temperatures, leading to structures typical for zone 2. The film consists of uniform columnar grains

reaching from the bottom to the top, separated by grain boundaries, which are nearly perpendicular to the surface.
Above a homologous temperature of 0.5, zone 3 appears, characterized by bulk diffusion or recrystallization, which results in larger globular grains in a polycrystalline structure [8, 11, 17, 18, 19, 20].

2.2.2 Substrate Bias Voltage

Another effective way to influence the coating deposition and as a consequence the film properties, is to apply a bias voltage (V_B) to the substrate, which means that it is held on a negative voltage referenced to the anode potential. Typically, the substrate bias is between 0 and -300 V, but can reach up to -10 kV in special implantation techniques. It allows the control and variation of the energy of the impinging ions and consequentially gives the possibility to vary coating morphology independently from the temperature. If energetic ions collide with the surface, different additional effects can occur, shown schematically in Fig. 2.7a. Where the ions hit surface atoms, they move them out of their lattice positions, causing further collisions and thus generating collision cascades, changing the defect structure of the material as seen in Fig. 2.7b. In [11] and [17] effects like higher nucleation rate and coating density, combined with smaller grain size and better surface finish, higher ad-atom mobility and desorption of residual gas ad-atoms are mentioned amongst others, making the energy of the incoming particles a very important factor to influence coating formation [8, 11, 15, 16, 17].

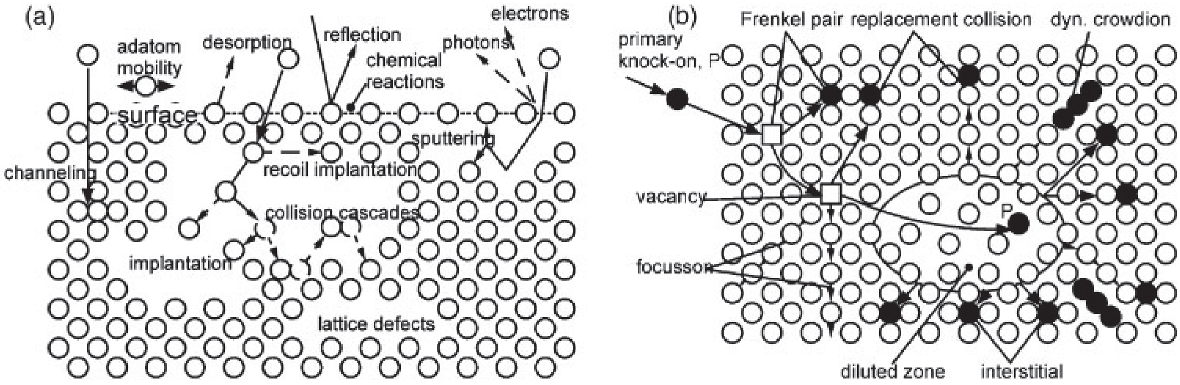

Fig. 2.7 (a) Effects of ion bombardment on a growing film in the 10–1000 eV range. (b) Overview of possible lattice defects caused by incident ions [16].

Bland et al. proposed a model where backsputtered and scattered particles fill up the otherwise shadowed areas, thus filling these voided zones, as shown in Fig. 2.8a. The influences of the V_B on sputtered coatings were studied and published by

Messier in the form of a revised structure zone model shown in Fig. 2.8b. Biasing does not affect the zones 2 and 3, because diffusion is already thermally activated. The favorable zone T emerges at the expense of the porous zone 1, when a certain V_B is applied. As a consequence the deposition temperature can be lower, enabling the use of other substrate materials. As the ions, accelerated by the bias potential, also sputter of deposited atoms the deposition rate decreases with increasing V_B [5, 6, 20, 22].

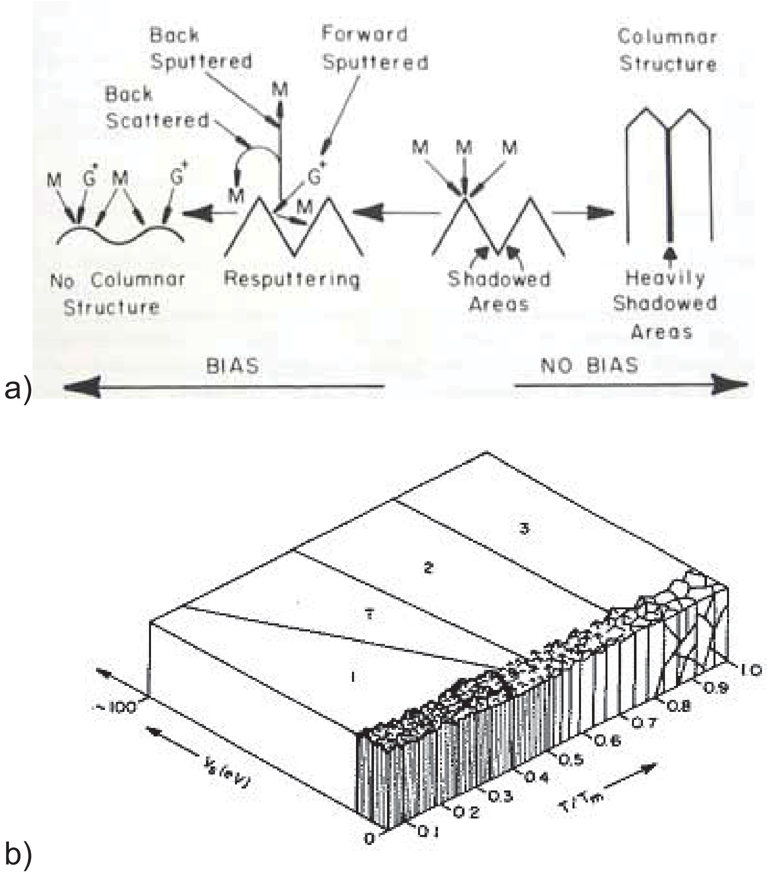

Fig. 2.8 (a) Growth modification by ion bombardment during deposition [6]. (b) SZM revised by Messier, taking the influence of V_B into account [22].

2.3 High Temperature Oxidation

In general chemistry, the term oxidation describes the loss of electrons by atoms, ions and molecules, or to be more precise, an increase of the oxidation number of the involved species. Although not generally valid, in this chapter the term will be used for reactions which lead to the loss of electrons and involve oxygen. On the other hand, a reaction leading to a gain of electrons is called reduction. The oxidation reactions considered here are of the type

$$xMe + 0.5(yO_2) \rightarrow Me_xO_y,$$

where Me can either be an atom of a pure metal or the metallic part of an intermetallic compound. Oxidation at a surface takes place in several steps, including the initial adsorption of oxygen, the chemical reaction followed by the nucleation of the oxide, and the lateral oxide growth into a continuous film. Fig. 2.9 illustrates these first steps. Afterwards, the oxide layer thickens and forms either a protective or nonprotective oxide film. The rate at which these steps occur is depending on the metal, the surrounding environment, the temperature and the formed oxide itself. Thus, the oxidation resistance of the material is determined by the whole system and not solely a property of the material investigated. At room temperature many metals are already oxidized, and thus covered by a protective layer, which is hindering or even preventing further oxidation. However at high temperatures the reaction rate increases rapidly leading to a fast degradation of the material, making the prevention of high temperature oxidation an important aspect in component and tool design [23, 24, 25].

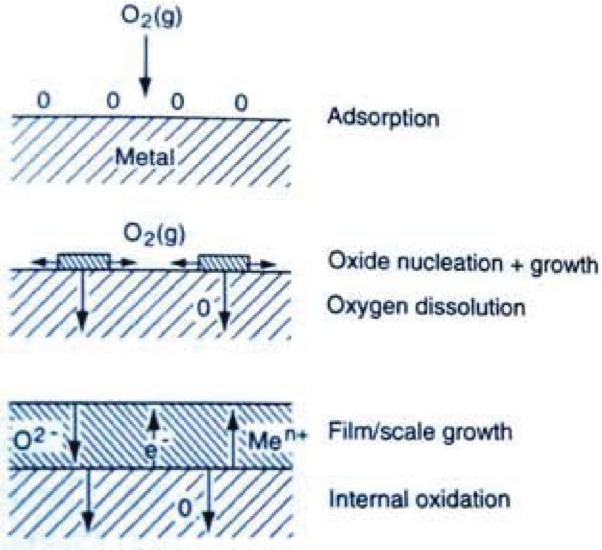

Fig. 2.9 The initial steps of oxide layer formation and growth [25].

If a stable oxide is formed, which means one that is chemically stable over the temperature range of interest, it can either remain bound to the metal surface or be volatile. Volatile oxides evaporate after being formed on the surface, leading to a mass loss and consequently no protection is provided by the already formed oxides. Technically important examples for this behavior are W, Mo and under certain conditions Cr. Oxides remaining on the surface protect it to some extent from further oxidation. The reason for this is the prevention of contact between oxygen and the unoxidized metal below the layer. The effectiveness of this protection mechanism depends on the rate of diffusion of the reactants through the oxide, and the supply of oxygen at the oxide layer surface, with the slowest of these steps being rate limiting. Furthermore, the molar volume of the oxide compared to the metal is of high interest. A molar volume of the oxide being larger than that of the metal, is needed to form an oxide layer, which covers the whole surface, but also poses the problem that stresses are induced during the scale growth. If these stresses exceed a critical value, cracking of the protective layer occurs and virgin metal is exposed to further oxidation, leading to a sudden increase of the oxidation rate. If these growth and cracking mechanisms occur periodically the behavior is called breakaway oxidation [25, 26].

When the oxide is formed on the surface of the metal, the oxidation rate can be determined by measuring the mass change over time. In the case of a stable adherent scale, oxidation is connected with a certain mass gain and increase in layer thickness, while volatile oxides are characterized by a mass loss. Three major types of dependencies between weight gain and time can be identified, which are plotted in Fig. 2.10.

The most common correlation between weight gain and time, found for many metals, is the **parabolic rate law**. Characteristic for this behavior is that the square of film thickness (x) is proportional to time (t), giving the equation

$$x^2=k_pt, \tag{2.1}$$

where k_p is known as the parabolic rate constant. An explanation of the controlling mechanisms has been given by Wagner and a detailed description of this theory is given in [26]. Wagner found that the diffusion of the different species through the oxide layer is rate controlling, when a compact and perfectly adherent scale is assumed. In this case the transport slows down propotionally to the increase of layer thickness [24, 25, 26].

Where a **linear rate law** is observed oxidation follows the equation

$$x=k_lt \tag{2.2}$$

with k_l being the linear rate constant. A linear law is usually found where a phase boundary reaction controls the reaction rate. Thus, the oxide layer must be nonprotective or is not covering the full surface, which can occur during the initial stages of oxidation. Also oxygen depleted atmospheres, as encountered during heat treatment under partial vacuum, are found to cause linear oxidation kinetics. For some materials oxidation starts following a linear rate law, afterwards changing to a parabolic dependence with increasing oxide thickness. At the same time pores and cracks may form, reducing the protection by the layer, with a resulting failure of the parabolic rate law. The outcome of this is again a linear dependency, which is called paralinear rate law. It has to be mentioned that the above discussed breakaway oxidation curve, where a parabolic oxidation rate is interrupted by periodical cracking and faster oxidation, evolves into a linear function for long time periods [25, 26].

The **logarithmic rate law**, being the third major type of kinetic rate law, often occurs for thin oxide films at rather low temperatures. It obeys the equation

$$x = k_e \log(a \cdot t + 1), \tag{2.3}$$

with k_e and a being constants. It is characterized by rapid oxide growth at the beginning of the oxidation process, which comes to a halt after reaching a certain layer thickness. Different assumptions were introduced to explain this behavior, basing the rate controlling mechanism on the influence of electric fields, the adsorption of reactive species and quantum mechanical tunneling of electrons through the growing scale [24, 25, 26].

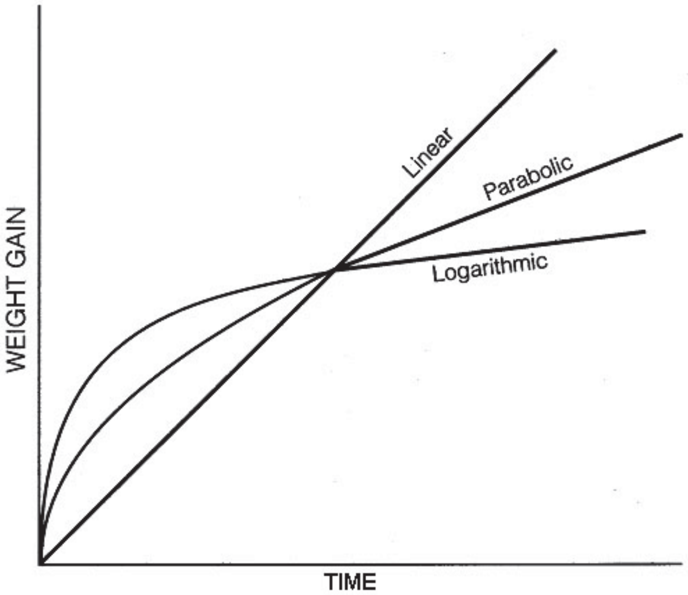

Fig. 2.10 Linear, parabolic and logarithmic oxidation rate laws for stable adherent oxides [25].

2.4 $Ti_{1-x}Al_xN$

In the mid-sixties TiN was introduced in the industry and since then it was one of the mostly used hard coatings for cutting and forming tools. The mixed nature of its atomic bonding, consisting partially of ionic, metallic and covalent components, gives rise to advantageous properties including high hardness, good wear resistance and chemical inertness. Limiting to the practical application of TiN is the relatively low oxidation resistance, with oxidation starting at temperatures as low as 550 °C in air. Against the background of the cutting industries demands for higher cutting speeds and lower coolant and lubricant consumption new coating materials were needed, which led to the development of $Ti_{1-x}Al_xN$ coatings. The incorporation of Al led to a considerable increase of the oxidation starting temperature and hardness while lowering the coefficient of friction [2, 15, 27, 29].

2.4.1 Microstructure of $Ti_{1-x}Al_xN$

The crystal structure of $Ti_{1-x}Al_xN$ is based on TiN, which crystallizes in the face centered cubic (fcc) B1 NaCl structure. The introduction of Al leads to a ternary coating system, for which the 1000 °C isothermal section of the phase diagram is shown in Fig. 2.11a. At the given temperature two phases are present in thermodynamic equilibrium, with the approximate compositions Ti_3AlN and Ti_2AlN. While the first one is of the cubic perovskite structure, the latter, also called H-phase, shows a hexagonal lattice [30, 31].

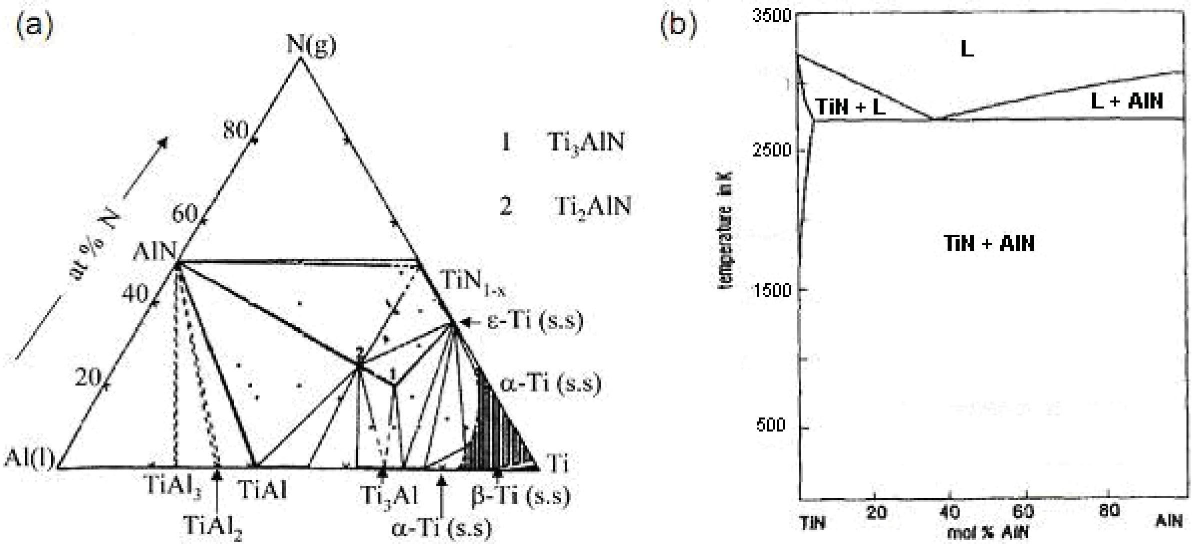

Fig. 2.11 (a) Ternary phase diagram of the system Ti-Al-N at 1273 K (1000 °C) [30]. (b) Quasibinary phase diagram of TiN-AlN [31].

Fig. 2.11b shows the quasibinary phase diagram of TiN and the hexagonal closed packed (hcp) AlN phase, where the very low solubility of the two phases in each other can be seen. At a temperature of 2700 K the maximum solubility for AlN in TiN is reached with about 5 mol%. At higher Al contents or lower temperatures the equilibrium composition consists of the separated fcc-TiN and hcp-AlN phases. PVD deposition techniques operate at low temperatures preventing pronounced diffusion over long distances and thus the formation of the equilibrium state. Due to this kinetic limitation and, in ion plating processes, enhanced by energetic ion bombardment, a metastable phase is formed, showing the same B1 NaCl structure as pure TiN. Depending on deposition technology and the chosen parameters this is possible up to certain Al contents. The lattice parameter decreases gradually from 4.23 Å for pure TiN to 4.17 Å on addition of Al. This suggests that the smaller Al atoms substitute Ti in the lattice, forming the metastable cubic $Ti_{1-x}Al_xN$ structure shown in Fig. 2.12 [27, 30, 31, 32, 34, 47].

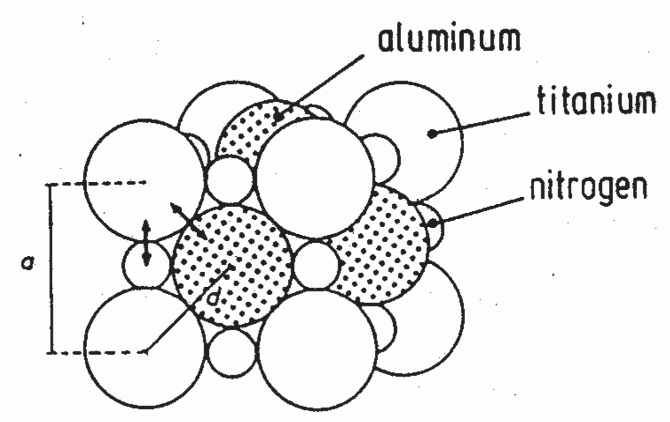

Fig. 2.12 Drawing of the fcc-TiN monocell with embedded Al atoms [41].

At high Al fractions a phase transformation can be observed, changing the crystal structure from the fcc NaCl structure of TiN to the hcp wurtzite structure of AlN. The values for the Al content where this transition occurs vary with the deposition technology used and so different values have been proposed in literature. Cremer et al. [42] calculated and experimentally approved a metastable quasibinary TiN-AlN phase diagram for the reactive magnetron sputtering ion plating (MSIP) process, which is shown in Fig. 2.13 [22, 42].

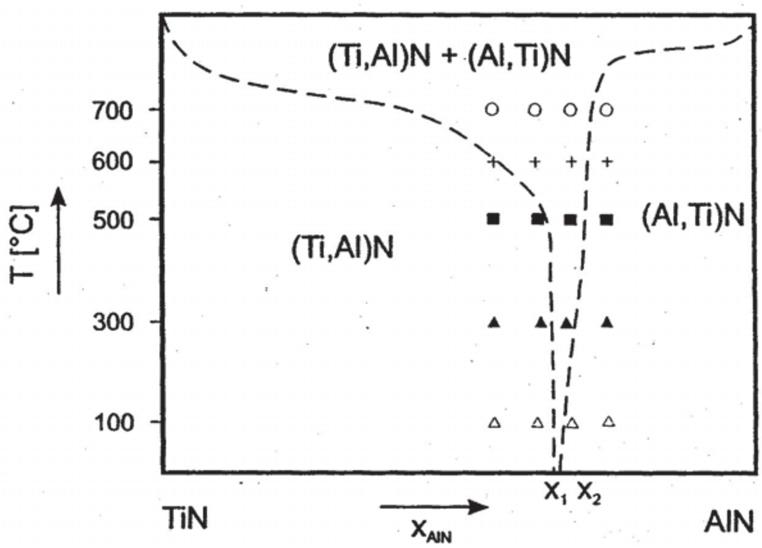

Fig. 2.13 Metastable TiN-AlN phase diagram for MSIP [42].

Between the single phase regions a two phase area can be found, which expands with increasing temperature but is narrow for typical PVD process temperatures. At 100 °C no two phase zone is observed and transition occurs between an Al content of $0.63<x<0.69$. For cathodic arc evaporation quite similar results were reported by Kimura et al. [43], who found that the phase transformation starts at $x>0.6$ and leads to hcp-AlN like crystals for $x>0.7$, with a two phase zone, consisting of a fcc- $Ti_{1-x}Al_xN$/hcp-AlN dual phase structure, in between [42, 43].

2.4.2 Mechanical Properties and Deposition of $Ti_{1-x}Al_xN$

The mechanical properties of $Ti_{1-x}Al_xN$ coatings are dependent on different factors like chemical composition and various deposition parameters. The influence of the Al content on coating hardness was investigated by several authors. They observed an increase of the hardness values with increasing aluminium content, as long as the films had a fcc single phase structure. Hardness increased from ~20 GPa for pure TiN to a maximum of ~31 GPa for 60 at.% Al (see Fig. 2.14), while the lattice parameter decreased as described before. As soon as the hcp-AlN phase occured and a dual phase structure was observed, hardness dropped. The same behavior was found for the Young's modulus of the coatings [30, 34, 43, 44, 46].

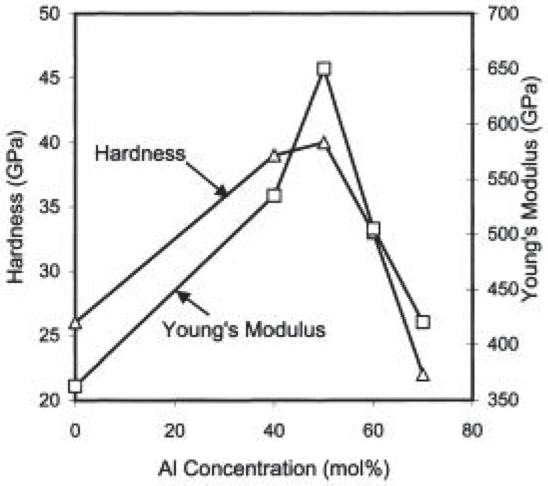

Fig. 2.14 The influence of Al content on hardness and elastic modulus [30].

The influence of V_B on the microstructure and properties of coatings deposited by CAE and using a $Ti_{30}Al_{70}$ cathode was analyzed by Kale et al. [45]. The reduction of the Al content in the coating, with increasing V_B is shown in Fig. 2.15a. This was explained by the higher degree of ionization of the Ti atoms (80%) compared to Al (50%) leading to a preferred attraction of Ti-ions to the substrate by the applied V_B and finally results in a change of the deposited Ti/Al ratio. In addition, a higher fraction of the lightweight Al atoms is resputtered in comparison with the heavier Ti atoms.

V_B also influences the phase composition of the coatings. An increase of the bias potential promotes the formation of the fcc-$Ti_{1-x}Al_xN$ phase suppressing the development of the hcp-AlN structure. Mayrhofer et al. [39] found, by ab-initio calculations, that the solubility limit of Al in fcc-$Ti_{1-x}Al_xN$ is dependent on the Al distribution in the metal sublattice. Higher Al contents can be incorporated in the metastable fcc single phase, when the number of Ti-Al bonds is decreased, and a low energy configuration, with Ti- and Al-rich sublattice areas, is formed. The higher ad-atom mobility, caused by V_B, might allow the formation of this structure, resulting in higher Al fractions built into the fcc structure. An additional effect contributing to the preferred formation of the fcc phase, takes the residual stresses into account. The residual compressive stresses, which increase with increasing V_B, may enhance the formation of the densest possible phase, which is fcc in this case.

Hakansson et al. [27] observed a reduction of porosity and grain size when comparing coatings deposited with a rather low V_B to unbiased ones, which led to an increase of hardness due to grain size hardening. They furthermore observed that higher V_B values led to an increased generation of lattice defects caused by the ion bombardment and thus to an increase of the compressive residual stresses in the coatings, leading to increased hardness again. Thus raising V_B increases hardness only until too many Al atoms are resputtered, or diffusion contolled mechanisms lead to enhanced relaxation, by annihilation of defects and hardness drops to levels comparable with lower Al contents (see Fig. 2.15b) [27, 30, 33, 39, 40, 45].

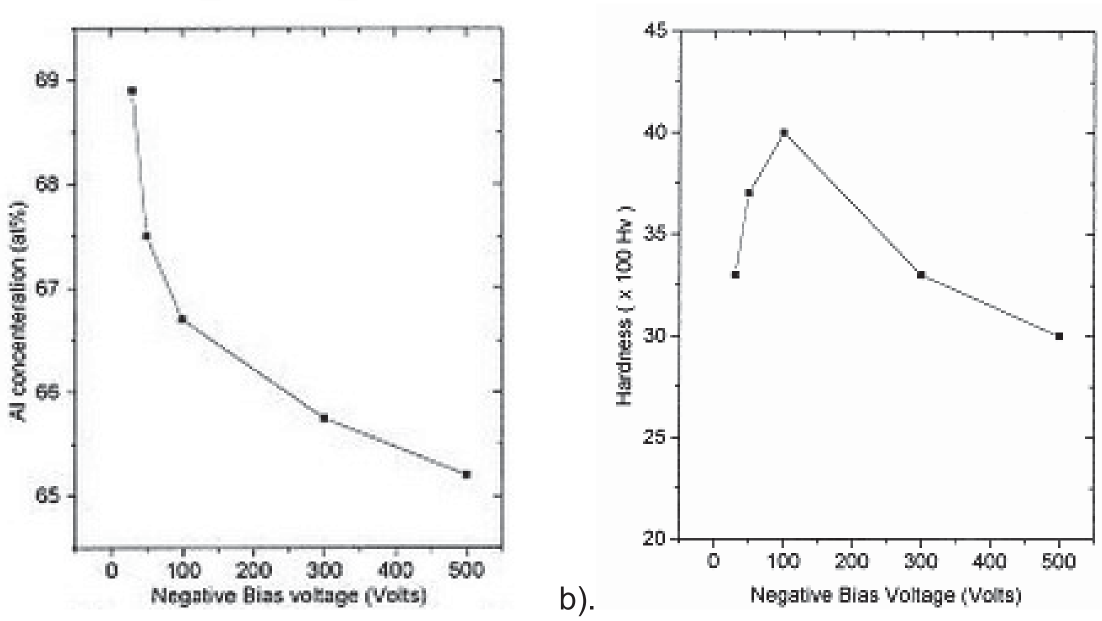

a). b).

Fig. 2.15 Influence of V_B on (a) the Al content and (b) the hardness of arc evaporated coatings [45].

The point defects introduced by ion bombardement cause compressive residual stresses in the coatings, which increase with higher V_B, due to the increasing number of point defects created. At the same time the energy put in by the ion irradiation enhances ad-atom mobility, whereupon diffusion controlled relaxation mechanisms annihilate point defects, lowering the residual stresses, if sufficiently high bias voltages are applied. The compressive stresses lead to increased hardness due to the higher resistance to crack initiation and enhanced crack closure mechanisms. Ljungcrantz et al. [35] measured the residual stresses for TiN coatings, deposited by CAE, and found values corresponding to those of a model proposed by Davis (see Fig. 2.16). The model developed by Davis assumes a steady state behavior of the defect creation by impinging ions and annihilation of the point defects by diffusional processes. The model was furthermore qualitatively confirmed by Oden et al. [37] for CrN coatings [35, 36, 37].

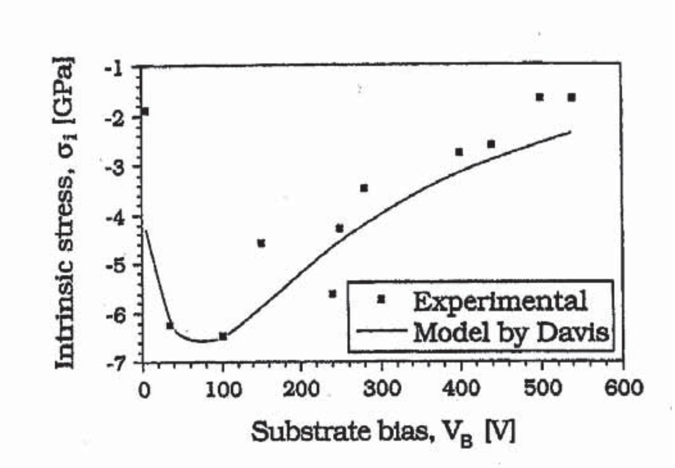

Fig. 2.16 Variation of the calculated and experimental intrinsic stresses with bias voltage modified after [35].

A change in the preferred orientation of TiN and $Ti_{1-x}Al_xN$ caused by the V_B was reported by Petrov et al. [18]. The texture changes from a preferred (111) to (002) orientation, when increasing ion energy. This behavior might be related to effects originating in the anisotropy of the collision cascades. Another explanation was proposed by Gall et al. [38], which links the texture changes to differences in the diffusivity on the surface of different orientations [18, 38].

2.4.3 Thermal Stability of $Ti_{1-x}Al_xN$

Annealing or the application of $Ti_{1-x}Al_xN$ coatings at high temperatures, might provide sufficient energy to enable decomposition of the metastable phases into the equilibrium fcc-TiN and hcp-AlN phases. Hörling et al. [47] performed annealing experiments on cubic $Ti_{34}Al_{66}N$ coatings. They observed assymetrical peak broadening in their XRD patterns after annealing the samples at 900 °C and hence concluded that spinodal decomposition of the coating took place. These results were later confirmed by DSC measurements as published by Mayerhofer et al. [47, 48].
The phase separation includes an intermediate step where the $Ti_{1-x}Al_xN$ solid solution separates as following:

$$\text{fcc-}Ti_{1-x}Al_xN \rightarrow \text{fcc-TiN} + \text{fcc-AlN}$$

This first step is necessary because the direct precipitation of hcp-AlN is unlikely due to the high nucleation barrier associated with the phase transformation. It results from the incoherent hcp-AlN/fcc-TiN interfaces and the about 20% larger atomic volume causing high stresses in the bulk material. In the second step, the coherent fcc-AlN transforms into the equilibrium hcp wurtzite structure. The complete transformation can be written as:

$$\text{fcc-}Ti_{1-x}Al_xN \rightarrow \text{fcc-TiN} + \text{fcc-AlN} \rightarrow \text{fcc-TiN} + \text{hcp-AlN}$$

The above described spinodal decomposition can only be observed in small temperature and composition ranges, while outside these, the more common process of phase separation by nucleation and growth of the hcp-AlN takes place [47, 48].

2.4.4 Oxidation Behavior of $Ti_{1-x}Al_xN$

The reason for the developement of new coating systems based on TiN was the poor oxidation behavior of the coating. TiN starts to oxidize in air at temperatures of 550 °C±50 °C as already mentioned before. At the onset of oxidation, oxygen starts to replace nitrogen and TiO_2, in the modification rutile, is formed on the surface of the coating. Nitrogen tends to be trapped inside the layer causing pores and allowing faster oxygen diffusion and increased delamination. Wittmer et al. [51] found that the oxidation of TiN in the range of 550 °C to 650 °C follows a parabolic time law, with an activation energy of 2.05 eV. Additionally the growing oxide layer introduces high compressive stresses in the coating, due to the difference in the molar volumes of rutile and TiN. These stresses increase with increasing layer thickness and at a certain level the oxide layer might spall of, exposing unoxidized TiN with the process starting again. Taking into account both parabolic oxidation and the periodic spallation of the oxide layer a resulting pseudolinear oxidation law is found [49, 50, 51].

The first ones reporting on the oxidation behaviour of $Ti_{1-x}Al_xN$ were Münz et al. [60], who found a significantly improved oxidation resistance for magnetron sputtered $Ti_{50}Al_{50}N$ coatings. The onset of oxidation is found to be at about 700 °C, but varies strongly with the coating composition. A comparison of the oxidation rate for TiN and a couple of different $Ti_{1-x}Al_xN$ coatings is given in Fig. 2.17 [28, 52, 30].

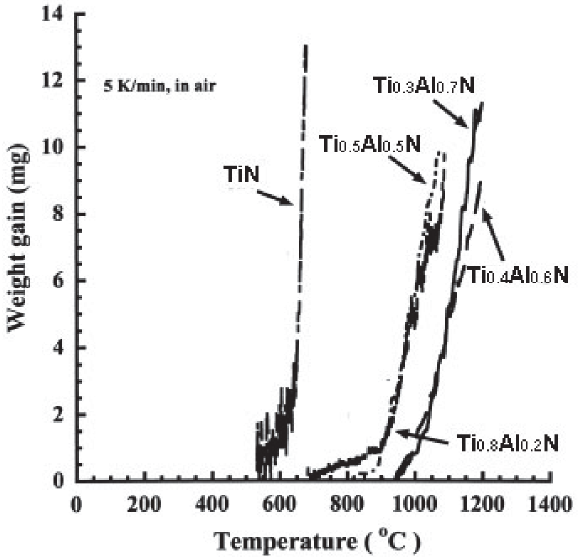

Fig. 2.17 Oxidation curves of $Ti_{1-x}Al_xN$ coatings with different Al contents compared to TiN [56].

The beneficial effect of Al is caused by a stable and protective layer of Al_2O_3 which is forming at temperatures of about 700 °C. The layer is highly insulating and dense, with low ion mobility and thus strongly limits the oxide growth by acting as an oxygen diffusion barrier. Increasing the Al content in the coating improves oxidation behavior as long as the coating crystallizes solely in the fcc-$Ti_{1-x}Al_xN$, as can be seen in Fig. 2.17. Irrespective of the dual phase structure occuring in the coatings containing 60 at.% Al and 70 at.% Al (compare Fig. 2.13), they show excellent oxidation behavior, which was unexpected as hcp-AlN is reported to have lower oxidation resistance than the fcc-$Ti_{1-x}Al_xN$ solid solution [3, 50, 52, 53, 56].

The composition of the oxide layer is not only dependent on the coating composition but also on oxidation temperature. Joshi et al. [57] found two different activation energies for different temperature ranges of the oxidation process, concluding a change of the oxidation mechanism between 700 and 800 °C. Above temperatures of about 800 °C the oxide layer separates into two sublayers. Already McIntyre et al. [52] observed that the oxide consists of an upper almost pure Al_2O_3 sublayer and a lower TiO_2 sublayer containing a few at.% of Al. In none of both any N was found. Inert marker experiments showed that Al diffuses to the oxide/environment interface and simultaneously the diffusion of O to the oxide/nitride interface takes place, as seen in Fig. 2.18a. At the present temperatures Al can diffuse rapidly through the TiO_2 interlayer to the surface, while the inward diffusion of O is impeded by the dense surface Al_2O_3 layer. Thus O diffusion is found to be the rate limiting step at the beginning of oxidation, following a parabolic growth law. As diffusion slows with increasing layer thickness, also the oxidation rate decreases, deviating from the parabola. Thus, the Al_2O_3 layer provides effective protection for the underlying coating. Due to the differences in molar volumes of the appearing phases, compressive stresses are introduced which can lead to the spalling of the layer or to the formation of cracks, by which oxidation can proceed a lot faster [52, 53, 54 , 55, 57].

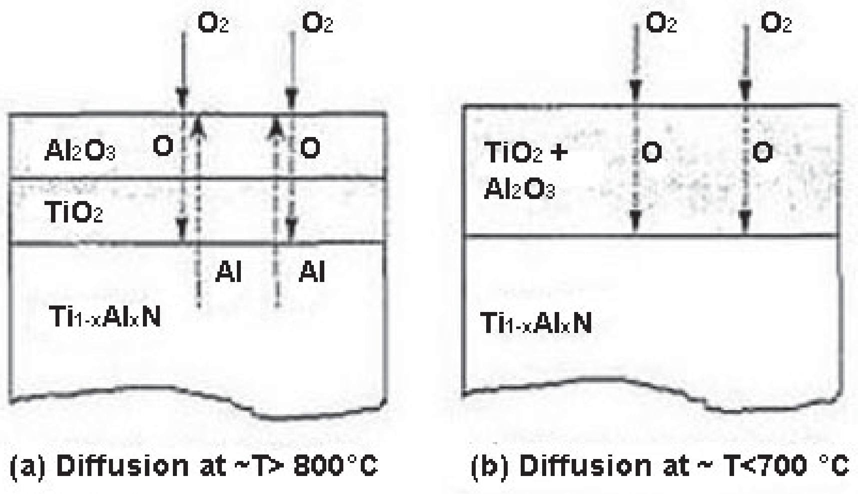

Fig. 2.18 Schematic illustration of O and Al diffusion in the high and low temperature ranges for $Ti_{0,5}Al_{0,5}N$ [modified after 57].

Below 700 °C a homogeneous oxide layer is formed, consisting of Ti, Al, O and for very low temperatures of around 550 °C, also about 10 at.% of N. The N can either be found, bound as an oxynitride $(TiAl)N_xO_y$ in the layer, or trapped as N_2 inside pores, but always vanishes at temperatures above 600 °C. The absence of the two-layered oxide structure can be related to the neglectable Al diffusion through the oxide in this temperature range. As only O can diffuse again, oxygen diffusion is the rate limiting step here, leading to a parabolic growth law again [53, 54, 57].

2.4.5 Alloying $Ti_{1-x}Al_xN$

As described above $Ti_{1-x}Al_xN$ improves the wear and thermal properties considerably when compared to TiN, but nevertheless it is sought to further enhance important parameters like hardness, oxidation resistance, the coefficient of friction or surface roughness. Various elements have been alloyed into $Ti_{1-x}Al_xN$ and the effects have been studied. Knotek et al. [58] tested the quarternary TiAlZrN system, as TiZrN had proven to be another promising advancement to TiN. Zr also forms stable oxides at high temperatures and contributes to solid solution hardening. As a result the oxidation resistance of TiAlZrN is as good as for $Ti_{1-x}Al_xN$ while hardness values of about 35 GPa are observed. Another positive effect of Zr, as for some other metals like V, Mn and Cr, is the ability to stabilize the fcc NaCl structure of $Ti_{1-x}Al_xN$, giving the possibility to increase the Al fraction of the coating and further increase hardness. The introduction of Y leads to distinct grain refinement due to continous nucleation and to an increase of hardness values caused by grain size hardening. Y segregates to the grain boundaries, inhibiting grain boundary diffusion during oxidation and therefore also improves oxidation resistance. Moser et al. [62] additionally observed, that Y promotes the formation of the hcp-AlN structure and thus decreasing hardness with increasing Y content. Kutschej et al. [63] investigated the effects of V introduction into $Ti_{1-x}Al_xN$ and found a decrease of the coefficient of friction at elevated temperatures of 700°C. This was attributed to the formation of V_2O_5, known to be a Magnéli oxide phase with easy shearable planes. The V contents of up to 25 at.% also stabilized the fcc-TiN structure, allowing the introduction of high Al contents, which lead to high hardness [30, 58, 59, 60, 61, 62, 63].

The grain size hardening (Hall-Petch-effect) of a material is a limited effect in nanocrystalline materials. Below a certain grain size softening (inverse Hall-Petch-effect) occurs, caused by grain boundary sliding. To avoid this behavior a strong interface can be introduced preventing the grain boundary motion. This principle consideration led to the development of superhard Ti-Al-Si-N coatings, as reported by Niederhofer et al. [64], with contents of 4 to 19 at.% and 2 to 11 at.% for Al and Si respectively. The highest measured hardness value for these coatings was about 60 GPa. This high hardness follows from the microsructure of the coating, consisting of nanocrystalline (nc) $Ti_{1-x}Al_xN$ surrounded by amorphous Si_3N_4. For high Si contents this structure also leads to improved oxidation behavior of the coatings, when compared to pure $Ti_{1-x}Al_xN$ for temperatures above 900°C, as reported in [3] by Vaz et al. [3, 64, 65, 66].

$Ti_{1-x}Al_xN$ coatings alloyed with B show a quite similar structure to the Si containing ones. In this case the deposited Ti-Al-B-N forms three phases, which are $Ti_{1-x}Al_xN$, BN and very low contents of TiB_2. Therefore it consists mainly of nc- $Ti_{1-x}Al_xN$ grains and an amorphous BN grain boundary phase separating the grains. Rebholz et al. [4] deposited coatings, with Ti/B ratios between 0.34 and 2.31, containing approx. 12-14 at.% Al, by electron beam evaporation. Inreasing hardness was observed with increasing B content. As such coatings have only about 12 at.% Al, no Al_2O_3 layer can be formed at high temperature which results in lower oxidation resistance in comparison to pure $Ti_{1-x}Al_xN$ [4, 30, 67, 68, 69].

3 Experimental

3.1 Coating Deposition

3.1.1 Deposition Facility & Parameters

Ceratizit Luxembourg (CTL) produced the coatings investigated in this thesis, using an Oerlikon-Balzers Rapid Coating System (RCS) deposition apparatus, which is an industrial scale multicathodic arc evaporation facility (see Fig. 3.1a). In Fig. 3.1b a possible arrangement of the six targets used during deposition is drawn, as well as the rotating carousel, to which the substrates were attached. For all deposition runs two pure Ti targets were used, besides four targets of the composition, which was aimed for to be deposited. Coatings of five different target compositions, which were $Ti_{33}Al_{67}$, $Ti_{32.5}Al_{67}Si_{0.5}$, $Ti_{31}Al_{67}Si_{2}$, $Ti_{32.9}Al_{67}B_{0.1}$ and $Ti_{32.5}Al_{67}B_{0.5}$, where the respective numbers give the contents of the different elements in the target in at.%, were deposited. Different bias voltages of -40 V and -160 V have been used for the deposition of each target composition. For all deposition runs cuboid-shaped silicon wafer pieces, with dimensions of 21 x 7 x 0.38 mm, were used as substrates.

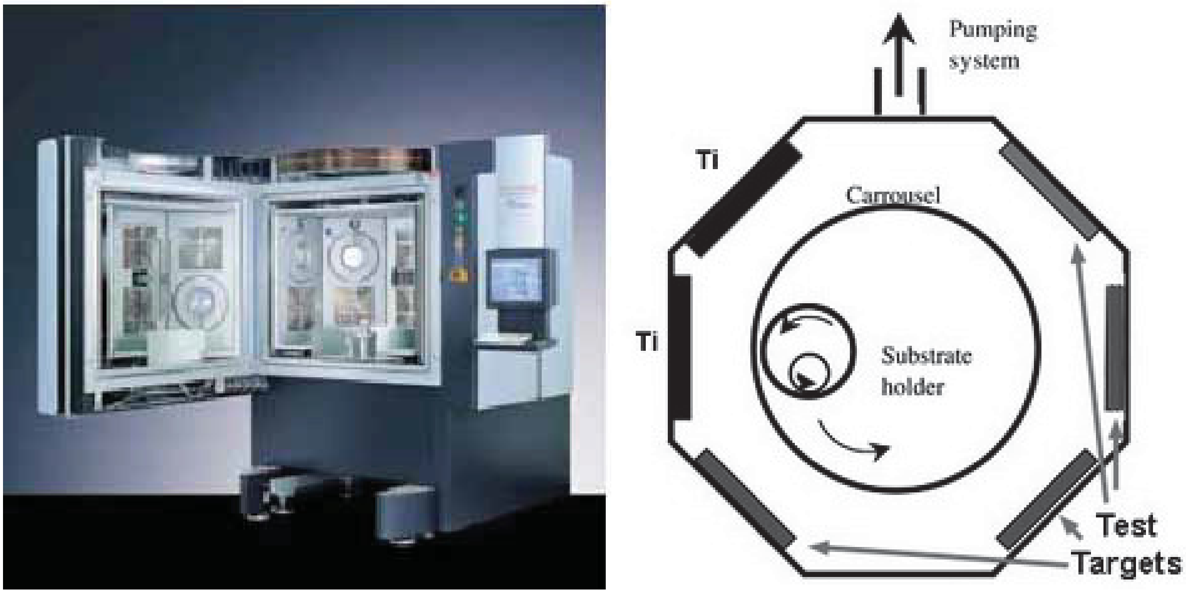

a) b)

Fig. 3.1 (a) Oerlikon-Balzers RCS deposition system, without the rotatable substrate holder [70]. (b) Schematic plan view of the deposition chamber showing the target arrangement and the possible rotations performed by the carousel [71].

3.1.2 Coating Work Cycle

The Si substrates were cleaned in ethanol and acetone in an ultrasonic bath, before being mounted onto the substrate holder, which was then put in the deposition chamber. In the coating process five steps can be distinguished. It starts with the evacuation of the deposition chamber, followed by heating, ion etching and the actual deposition. The process ends with the cooling of the samples.

The evacuation step leads to a pressure of approx. 10^{-5} mbar in the chamber, which is sufficient for the further process steps. Heating is conducted in two ways, first via radiation heaters inside the vacuum chamber and secondly by direct electron bombardment. In the latter case the electrons are accelerated away from an electron source, placed on top of the chamber, towards the anodic substrate holder and substrates. The impinging electrons transfer their energy to the substrates, thus heating them to the desired temperature. The substrate temperature used in this work was 450 °C for all coatings.

Ion etching follows heating and poses the last step of cleaning the substrate surface. In this process the substrates are switched as cathodes and the recipient as the anode. On the introduction of an inert gas, in this case Ar, into the chamber a plasma is ignited, and Ar^+ ions are created. By the anode-cathode potential these ions are accelerated towards the substrate, sputtering off the topmost layer exposing virgin substrate material, which is coated in the next step.

During the deposition process the only gas introduced is N_2, working as the reactive gas. At first only the two Ti targets are used to deposit a thin layer of TiN, which serves to improve coating adhesion. Afterwards the actual deposition process begins, when the other four targets, consisting of the composition which is to deposit, are ignited. During the deposition process the bias potential is provided by an additional power supply. The deposition time determines the coating thickness and was chosen approx. 6 hours for all coatings investigated in this work. The final step of the deposition process is to let the samples cool down in the deposition chamber, before unmounting them from the substrate holder.

3.2 Heat Treatment

Heat treatment was conducted to oxidize the samples for the subsequent characterization. The samples were anneald at 700 °C, 800 °C and 900 °C with a dwelling time of 30 min for all temperatures. Additionally, samples were heat treated at 900 °C for 60 and 300 min. Two annealing furnances, of the types Carbolite RHF 16/15 and Carbolite HRF 7/45, were used to carry out the annealing. The annealing conditions are listed together with the respective furnances in Table 3.1.

For the heat treatment the coated silicon wafers were scratched and afterwards broken, to obtain samples of 7 x 5 x 0.39 mm. These were put into crucibles and heated to the annealing temperature with a heat-up rate of 10 K/min. After holding the samples at the given parameters, they were cooled to room temperature in the furnance.

Table 3.1 Annealing temperatures and times together with the annealing furnance used.

Temperature [°C] :	700	800	900	900	900
Time [min]:	30	30	30	60	300
Annealing Furnance:	HRF 7/45	RHF 16/15	RHF 16/15	RHF 16/15	RHF 16/15

3.3 X-Ray Diffraction Analysis

Throughout the 20th century X-ray diffraction (XRD) has acted as a main method for the characterization of the internal structure of materials. Phase and texture analysis, as well as the determination of residual stresses and grain size are the main fields of application of this non-destructive method. Within this work XRD was used to determine the phase composition of the coated samples and its change, with respect to the influence of the heat treatment. Diffraction occurs when waves, in XRD X-rays, are scattered by an object and interfere constructively or destructively. The appearance of constructive interference, considering the periodicity of the crystalline lattice, is bound to the fulfillment of the Bragg condition [70]:

$$n \cdot \lambda = 2 \cdot d_{\mathrm{hkl}} \sin \Theta, \tag{3.1}$$

where n is an integer indicating the class of diffraction, λ terms the wavelength of the radiation, d_{hkl} is the interplanar spacing between two planes with the Miller indices h, k and l, while Θ stands for the diffraction angle.

In the present thesis, a Siemens D500 Diffractometer was used, which is operating with monochromatic X-rays of Cu K_{α} radiation and set up with the so called Bragg-Brentano geometry. In this case, the X-ray source is stationary, while the sample and the detector are moving, whereas the incident radiation strikes the sample at an angle of Θ, while the diffracted beam is detected at an angle of 2Θ. In order to maintain the fulfillment of Bragg's law, the detector has to move with twice the angular speed of the sample. This arrangement, schematically shown in Fig. 3.2, is called a Θ–2Θ scan and due to considerations concerning the scattering vector, the measurable lattice planes (hkl) are constrained to those lying parallel to the sample surface [70, 73].

Using the Bragg condition, peaks at certain values of 2Θ can be connected to a certain orientation, or more precise, its lattice spacing d_{hkl}. Thereupon the resulting interplanar spacing can be linked to known chemical compounds or elements, with their crystalline structures, which are tabulated as references. The measured peak positions and relative intensities obtained in this work, where compared to diffraction data stored in the JCPDS powder diffraction database. The parameters used for the XRD measurements are given in Table 3.2.

Table 3.2 Parameters used for the XRD measurements.

λ(Cu K_α) [Å]	K_β-Filter	Voltage [kV]	Tube Current [mA]	Step Time [s]	2θ Step [°]	2θ Range [°]
1.54056	Ni	40	25	1.2	0.02	15-85

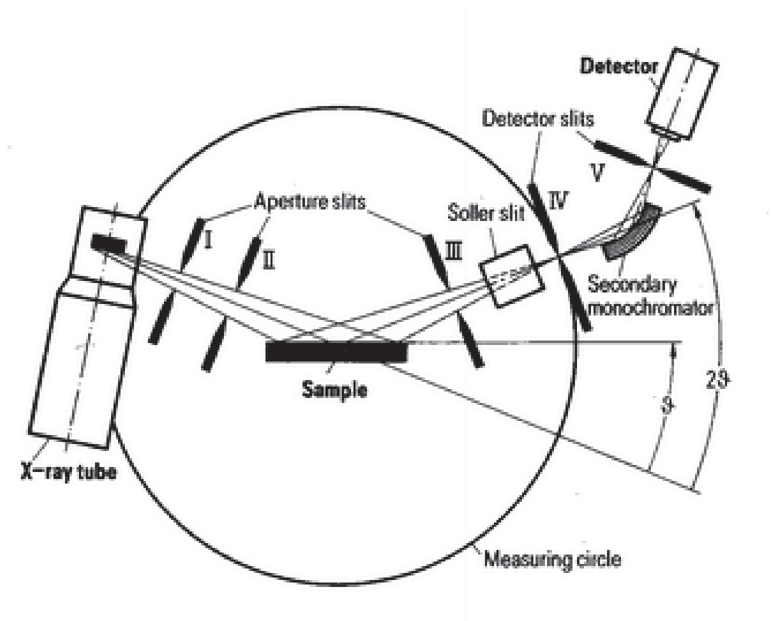

Fig. 3.2 Schematic of an XRD with Bragg-Brentano configuration [70].

3.4 Raman Spectroscopy

Raman scattering and the Raman effect are associated with the inelastic scattering of light by most of the elementary excitations possible in crystalline or amorphous solids. A quantum-mechanical model has been developed to describe the Raman effect. It is based on the interaction of the incident light quanta with quantized vibrational states of the crystal or molecule, which are called phonons in solid state physics. The energy, supplied by the absorbed light quanta, lifts the vibrational system to a virtual high-energy state, from where it will return to lower energetic states immediately. The energy difference between the high and low energy states is emitted as photons. In the case of elastic, or Rayleigh scattering, the emitted photons have the same energy as the supplied ones, as the system returns to the ground state, which is shown in Fig. 3.3a. If the phonons fall to an energetic state higher than the ground level (shown in Fig. 3.3b), photons with lower energies (E_S) are emitted, corresponding to the equation for the Stokes type of Raman scattering:

$$E_S = h(\nu_o - \nu_1), \tag{3.2}$$

where h designates Planck's constant, ν_o is the frequency of the absorbed photon and ν_1 the frequency corresponding to the energy of the involved phonon. For temperatures above absolute zero, it is also possible, that a before already excited phonon returns to a state lower than the original one and thus the emitted photon posesses a higher energy (E_{aS}) than the incoming ones. This behavior, shown in Fig. 3.3c is called an anti-Stokes process and can be described by the following equation:

$$E_{aS} = h(\nu_o + \nu_1) \tag{3.3}$$

Therefore the inelastic scattering process is connected to a shift in frequency and wavelength, which is characteristic for the excitational levels and thus the chemical and crystalline bonding structure, of the investigated material. This wavelength change, also called Raman shift, is measured and compared to known and tabulated reference data [75, 76].

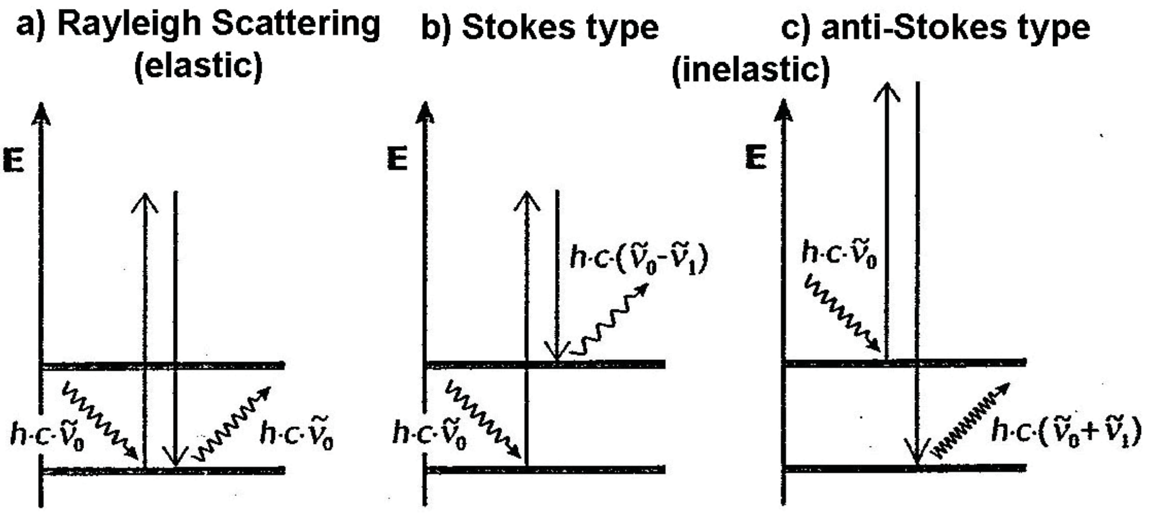

Fig. 3.3 Possible photon-phonon interactions with a) elastic Rayleigh scattering and the inelastic Raman scattering types b) Stokes and c) anti-Stokes [75].

Raman spectroscopy provides good lateral resolution and very good surface sensitivity, which makes it an interesting method for the characterization of thin films. The measurements in this work where carried out using a Jobin Yvon LABRAM confocal Raman spectrometer. It operates with a frequency doubled Nd-YAG laser, with λ=532.5 nm and a power of 100 mW. Further details on the used equipment, which is shown in Fig. 3.4, can be found in [76].

Fig. 3.4 The Raman spectrometer used for the measurements in this thesis [76].

3.5 Scanning Electron Microscopy

Fracture cross-sections of the as-deposited and annealed samples were investigated with a scanning electron microscope (SEM), of the type Zeiss Evo50 SEM. The coating morphology and thickness as well as the development and thickness of the oxide layer were examined, with secondary electron (SE) and quadrant back scattering detector (QBSD) imaging modes. Secondary electrons only travel distances below 10 nm in the specimen, due to their low energies of 0 to 50 eV, thus they are emitted from a small surface-near escape region. Due to their nature, they carry information on the surface topography, which when displayed results in images with high resolution [77, 78].

The latter mode, QBSD, is based on the detection of back scattered electrons (BSE), which have energies higher than 50 eV. The number of BSE emitted is dependent on the atomic number Z of the specimen, monotonically rising with rising Z. Thus it can be used to determine areas with different chemical compositions, separating regions with high and low average atomic number. As a result of their higher energy, the BSE are emitted from a larger specimen volume, which can be about 1 μm^3 or even more. Consequently the BSE contain more information on the volume than on the surface of the sample, resulting in lower contrast of the surface topography. Hence SE mode is used to examine the sample topography, whereas QBSD is used to identify different phases, such as oxides, in the sample [77, 78].

Additionally energy dispersive X-ray spectroscopy (EDX) was used to obtain qualitative information on the chemical composition of the samples. The system used was an Oxford Instr. INCA EDX attached to the SEM and calibrated with a Co-standard.

3.6 Transmission Electron Microscopy

3.6.1 General Considerations

Many properties of materials are determined by their microstructure. To picture the crystalline structure of these materials light microscopy is improper, due to the low resolution limited by the wavelength of visible light (λ=3800 Å). The use of electrons allows the variation of the wavelength with the applied acceleration voltage E_A, reaching wavelengths of λ=0.037 Å at E_A=100 kV. Transmission electron microscopy (TEM) uses this advantage of electrons over visible light, to generate images with a resolution of the order of 5 Å [77, 78].

In TEM a focused and highly coherent electron beam is incident on a very thin sample. Both deflected and undeflected electrons are detected and contribute to the signal, which is then displayed on a detector, usually a fluorescent screen or CCD camera. Depending on the atomic number of the sample material, the probe has to have a thickness between 20 to 300 nm to be transparent for electrons, which demands extensive and complex sample preparation [77, 79].

Besides taking images of the permeable sample region, TEM also allows to record diffraction patterns of an illuminated sample area. The obtained pattern is called selected area electron diffraction (SAED) and is completely equivalent to an XRD pattern. A SAED pattern is analyzed similar to an XRD pattern and is also often used to obtain the interplanar spacing and subsequently the Bravais lattice of a material [78, 79].

A PHILIPS CM 12 TEM, shown in Fig. 3.5, was used to investigate the samples in this work. E_A was 120 kV and a CCD camera (GATAN Model 794 MSC BioScan) was used as detector. Bright field images were made and additionally SAED patterns were recorded for selected regions.

Fig. 3.5 PHILIPS CM 12 TEM used to examine the samples in this work [80].

3.6.2 Sample Preparation

Aim of the TEM investigations was to obtain information on the coating structure and morphology as well as to gain deeper knowledge on the structure and composition of the oxide layer found on the annealed samples. Thus it was decided to prepare cross-sectional samples, as it should be possible to obtain all the requested information with a single sample of each tested coating. The preparation involved the following steps:

- The coated and annealed samples are scratched and afterwards broken into prisms with dimensions of approx. 1 x 0.38 x 7 mm.
- Two of these prisms, taken from the same as-deposited or oxidized sample, are glued together with the coatings facing towards each other, using a two-component adhesive (Measurements Group Inc.® M-Line M-Bond 610 Adhesive Kit).
- The thus created arrangement is cured for 120 min at 160 °C, resulting in a chemically and thermally inseparable sample-adhesive-sample-sandwich.
- The sandwich is coarsely pregrinded with an abrasive paper, until it is flat enough to stand upright on one side, perpendicular to the adhesive film.
- This side is then glued to a glass plate, which itself is bonded to a tripod, with a wash away adhesive (Testbourne Ltd. Quickstick 135), which was melted before at about 150 °C.
- The tripod polishing technique is used to hold and balance the sample, to achive a flat and equally thick specimen. The sample thickness is halved by grinding, using diamond abrasive films with grid sizes of 6, 3 and 1 µm and

afterwards polished with a 0.25 µm oxide polishing suspension (Struers® OP-S™).

- This procedure is then repeated for the backside of the sample which is subsequently grindend down to a final thickness of approx. 30 µm, using the same arrangement of grinding and polishing. This procedure should guarantee a good surface finish on both sides and a plane-parallel specimen.
- The glass plate with the hence finished sample is taken off the tripod. Afterwards the glass plate and sample are separated by dissolving the adhesive in acetone.
- The still 7 mm long sandwich is broken into parts, with a length of approx. 2 mm. Each thus created part is then bonded to a 30 µm thick, long hole copper TEM-grid, using the M-Bond 610 adhesive. The grid has an outer diameter of 3.05 mm and an inner slot of 2 x 1 mm, limiting length of the sample pieces to values between 1 and 3 mm.
- The final step of sample preparation is ion milling. Therefore a PIPS-device (Gatan 691 Precision Ion Polishing System) is used to further thin the specimen, by sputtering a half moon shaped hole into the sandwich, with the edges of this shape being the areas of interest. The edges of this hole are thin enough to be transparent for the accelerated electrons of a TEM.

4 Results

In this chapter the results for the tested coatings will be summarized for Ti-Al-Si-N and Ti-Al-B-N separately. It has to be mentioned that the given chemical composition of the coatings complies to that of the targets in at.%.

4.1 X-Ray Diffraction

4.1.1 Ti-Al-Si-N

As-deposited state

The results of the XRD investigations of the Si-alloyed coatings are shown in Fig. 4.1 and Fig. 4.2, whereas Fig. 4.1 shows the results of -40 V and Fig. 4.2 of -160 V bias voltage. For comparison the patterns for unalloyed $Ti_{33}Al_{67}N$ are also included. The shown droplines indicate the peak positions of fcc-TiN (2Θ= 33.66°, 42.6°, 61.81°), fcc-AlN (2Θ= 37.79°, 43.92°, 63.83°) and hcp-AlN (2Θ= 33.22°, 36.04°, 49.82°, 59.35°) in blue, green and red, respectively. In Fig. 4.1 the peaks detected around 37°, 43°, and 63° originate from fcc phases. The presence of these coating peaks between those of the fcc-TiN and fcc-AlN allows the assumption that none of the two phases is found purely but a $Ti_{1-x}Al_xN$ solid solution is formed. This phase can be described as TiN with smaller Al atoms built in, which causes a shrinking lattice and shifts the peaks to higher 2Θ angles, or AlN with embedded larger Ti atoms displacing the peaks to lower values. The peak at values of $2\Theta \approx 33.6°$ is associated with the hcp-AlN peak at 36.04°, which is also shifted to lower values due to the Ti content of the phase. This hcp-AlN peak gets stronger with increasing Si content, which allows the conclusion that Si promotes the hcp phase formation. No evidence for other phases like Si_3N_4 was found.

Increasing the bias voltage to -160 V leads to a supression of the formation of the hcp-AlN phase, which can be seen by the absence of the hcp peak at around 35°. Fig. 4.2 shows that the originally fcc-$Ti_{1-x}Al_xN$/hcp-AlN dual phase structure of the $Ti_{33}Al_{67}N$ in Fig. 4.1 has changed to a single phase fcc structure, due to the influence of the increased bias voltage. The same trend is observed for the 0.5 at.% Si containing coating. Only in the pattern recorded for $Ti_{31}Al_{67}Si_2N$ the hcp-AlN phase is still found, which can be seen at 34° as a shoulder to the neighboring fcc peak. The small peak found at approx. 57° can be linked to the hcp-AlN peak at 59.35°, confirming the assumption that Si promotes the hcp phase formation.

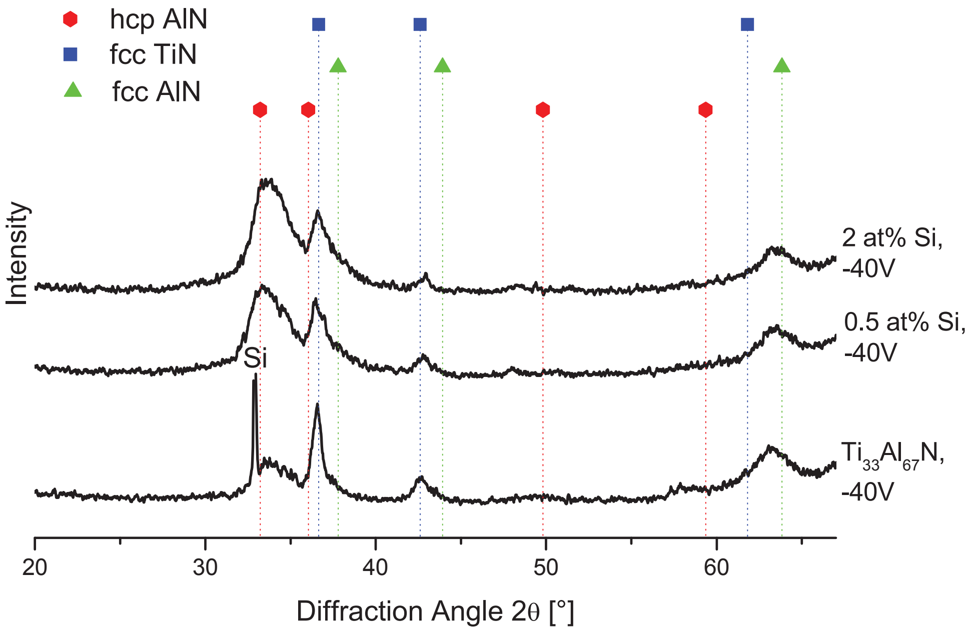

Fig. 4.1 XRD patterns of the as-deposited Si alloyed coatings with V_B=-40 V, on Si substrates, compared to the reference $Ti_{33}Al_{67}N$ system.

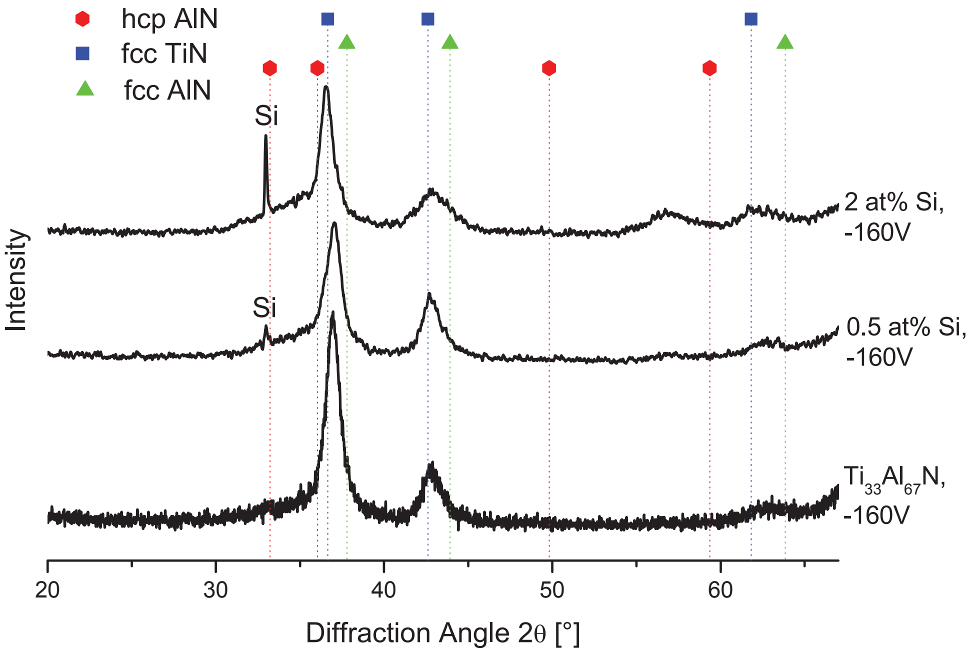

Fig. 4.2 XRD patterns of the as-deposited Si doped coatings, grown on Si substrates, compared to the reference $Ti_{33}Al_{67}N$ system coated with V_B= -160V.

The oxidized state

According to the description in chapter 3 all coating systems were oxidized in air at temperatures between 700 °C and 900 °C for 30 to 300 min. Fig. 4.3 shows the results for the system $Ti_{31}Al_{67}Si_2N$, deposited with -40 V bias, after oxidizing and in the as-deposited state. To ease the comparison with the reference material, the curves of the pure $Ti_{33}Al_{67}N$, V_B=-40 V, sample annealed at 900 °C for 60 min and 300 min are also shown. In addition, droplines of the peak positions of Al_2O_3, corundum and of the TiO_2 modification rutile are plotted in pink and black, respectively.

For $Ti_{31}Al_{67}Si_2N$ no oxide peaks can be identified before annealing the samples at 900 °C for 60 min. When annealing with these parameters, an Al_2O_3 peak appears at 25.4° indicating the presence of a formed oxide layer. When annealing for 300 min at 900 °C, this peak gets stronger with another corundum peak appearing at 43.4°. In addition, rutile peaks appear at 27.5° and 44.3°. Nevertheless, for both holding times the nitride peaks of the original coatings can still be observed.

Because of a superposition of the higher compressive stresses in the -160 V biased coatings with thermal stresses introduced by the heat treatment, some of these coatings spalled of or fractured, which made XRD measurements impossible. Nevertheless, the incomplete data of the oxidized samples showed the same trend as the -40 V biased coatings.

Oxidizing the $Ti_{33}Al_{67}N$ reference for 60 min at 900 °C already brings forth corundum peaks at 25.64°, 35.24°, 38°, 43.4°, 52.6°, 57.54°, 66.54° and rutile peaks at 2Θ angles of 27.52°, 36.2°, 54.56°, 62.86°, which are present together with the nitride reflections. The reference $Ti_{33}Al_{67}N$ specimen held at 900 °C for 300 min does not exhibit any nitride peaks anymore, suggesting that the original coating has decomposed completely into corundum and rutile. It has to be mentioned that the absolute intensities of the patterns can not be compared, as the irradiated area of the tested specimens varies, due to differences in the sample size.

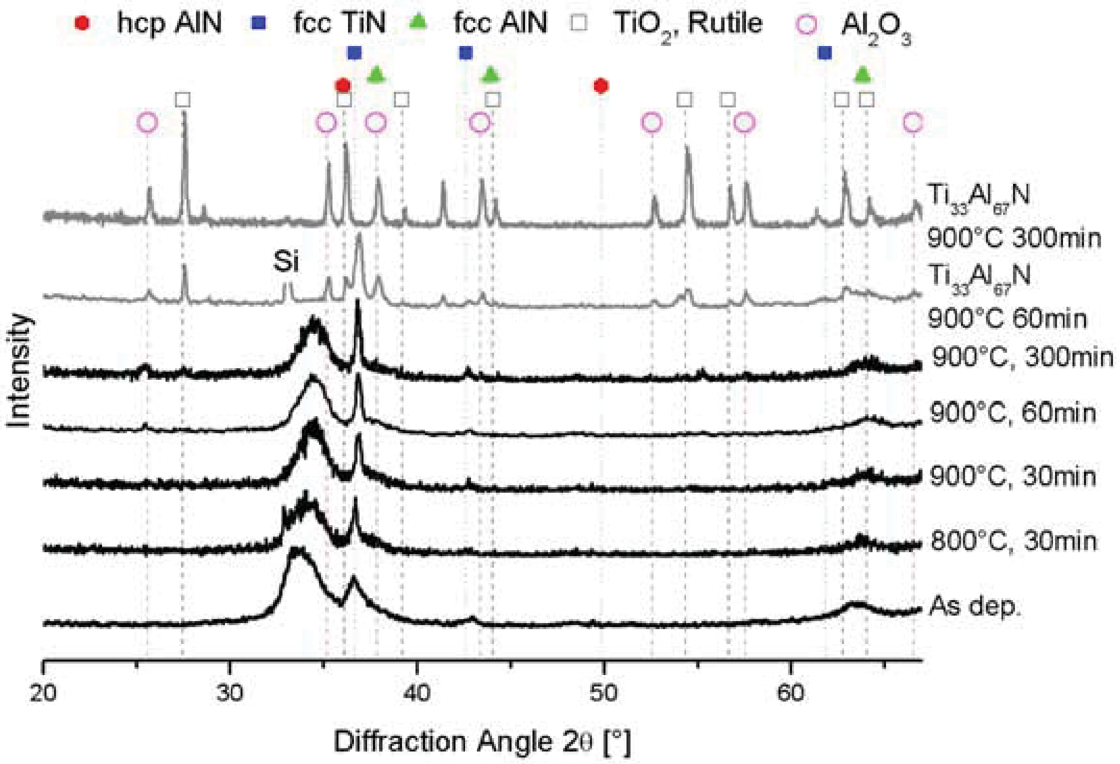

Fig. 4.3 XRD patterns for the different annealing states of $Ti_{31}Al_{67}Si_2N$ on Si substrates, V_B= -40 V, compared to $Ti_{33}Al_{67}N$ annealed for 60 and 300 min at 900°C.

4.1.2 Ti-Al-B-N

As-deposited state

In Fig. 4.4 the patterns of the B alloyed coatings, deposited at V_B=-40 V, are shown.
Besides the substrate peak at ~33.2°, peaks of metastable fcc-$Ti_{1-x}Al_xN$ are found, lying between the droplines of fcc-TiN and fcc-AlN. For all chemical compositions deposited, a hcp-AlN peak is found at approx. 34°. The fraction of the hcp-AlN increases with increasing B content in the coatings, at the same time lowering the contents of the fcc solid solution. This allows the conclusion that also B promotes the formation of the hcp-AlN phase.
Applying a higher V_B of -160 V leads to a solely fcc-$Ti_{1-x}Al_xN$ solid solution for the unalloyed $Ti_{33}Al_{67}N$ coating as well as for the coating alloyed with 0.1 at.% B, as shown in Fig. 4.5. No hcp-AlN peak is observed at ~34°, indicating that the applied V_B suppresses the formation of this phase. The pattern of the system containing 0.5 at.% B shows a small shoulder at $2\Theta \approx 34°$ indicating the presence of some remaining hcp-AlN phase. No borides were found, which leads to the assumption that the low B contents used are in solid solution.

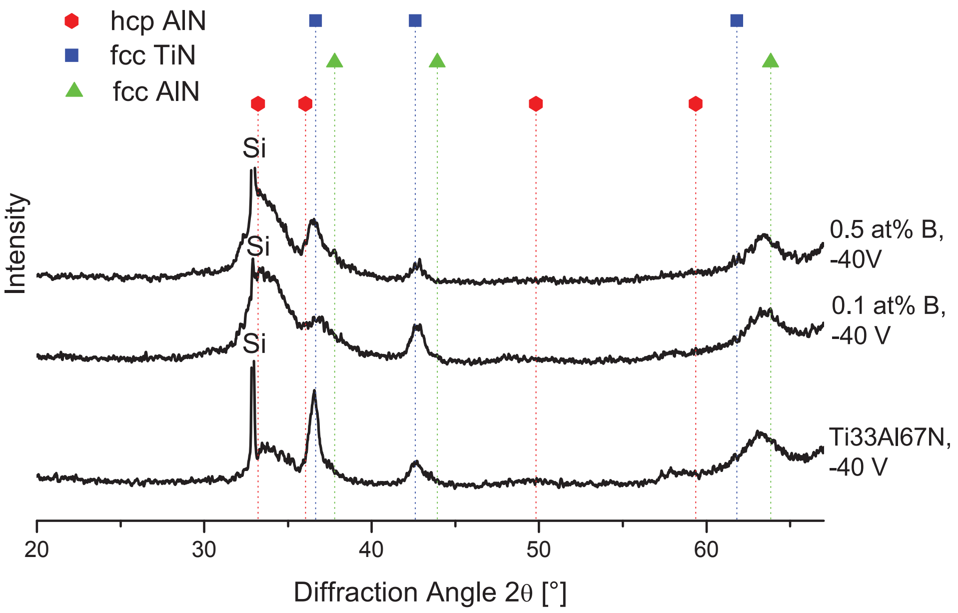

Fig. 4.4 XRD patterns of the as-deposited B-alloyed coatings with a V_B of - 40V on Si substrates. Additionally the pattern of unalloyed $Ti_{33}Al_{67}$, V_B=-40 V, is shown.

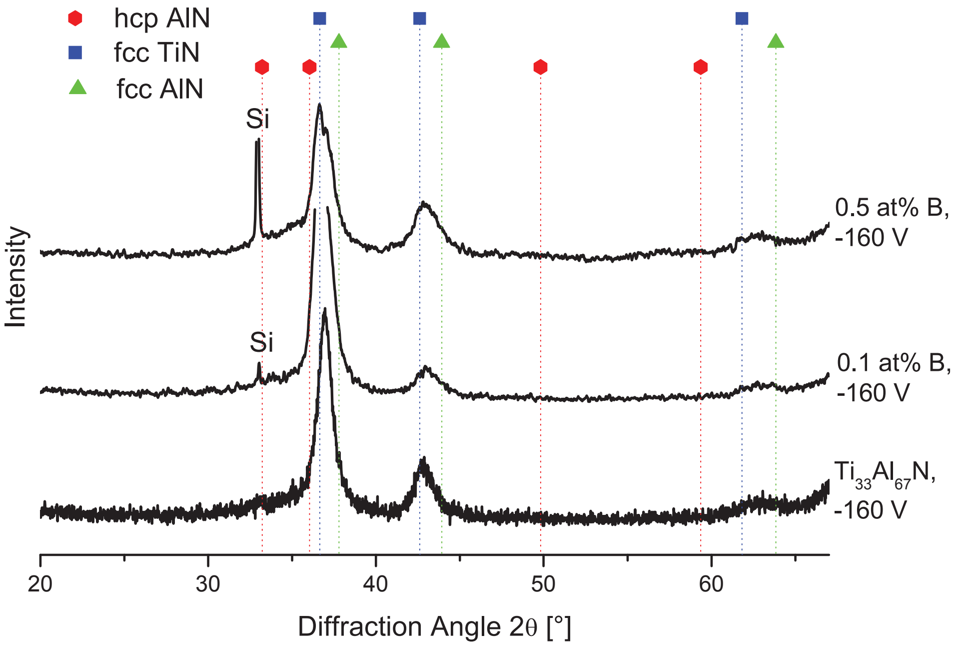

Fig. 4.5 XRD patterns of the as-deposited B alloyed coatings on Si substrates, with $Ti_{33}Al_{67}N$ as reference material, deposited with bias voltages of V_B= -160 V.

The oxidized state

When analyzing the recorded XRD patterns, the first signs of beginning oxidation are found after annealing the B alloyed coatings (V_B=-40 V) for 30 min at 900 °C, where peaks appear at 22.58°, 27.48° and 54.26°. The first one can be assigned to corundum and the latter ones to rutile. The specimen held for 60 min at the highest temperature shows a strengthening of the already appeared peaks and the appearance of further peaks of rutile and corundum, although still both cubic and hexagonal nitride phases are present. The most severe annealing conditions, 900 °C for 300 min, led to the complete transformation of the original coating into oxides. No nitride peaks can be found in the pattern anymore and all appearing reflections can be assigned to Al_2O_3 and TiO_2. The B alloyed coating exhibits the same structure as the unalloyed $Ti_{1-x}Al_xN$ after the longest holding time. No quantitative statements can be made regarding the patterns, due to differences in the sample size and consequently the irradiated area. As mentioned above, due to failure of many of the -160 V biased coatings during oxidation, no complete set of XRD patterns could be obtained. Nevertheless, the available specimens showed a behavior similar to that of the samples deposited with - 40 V bias.

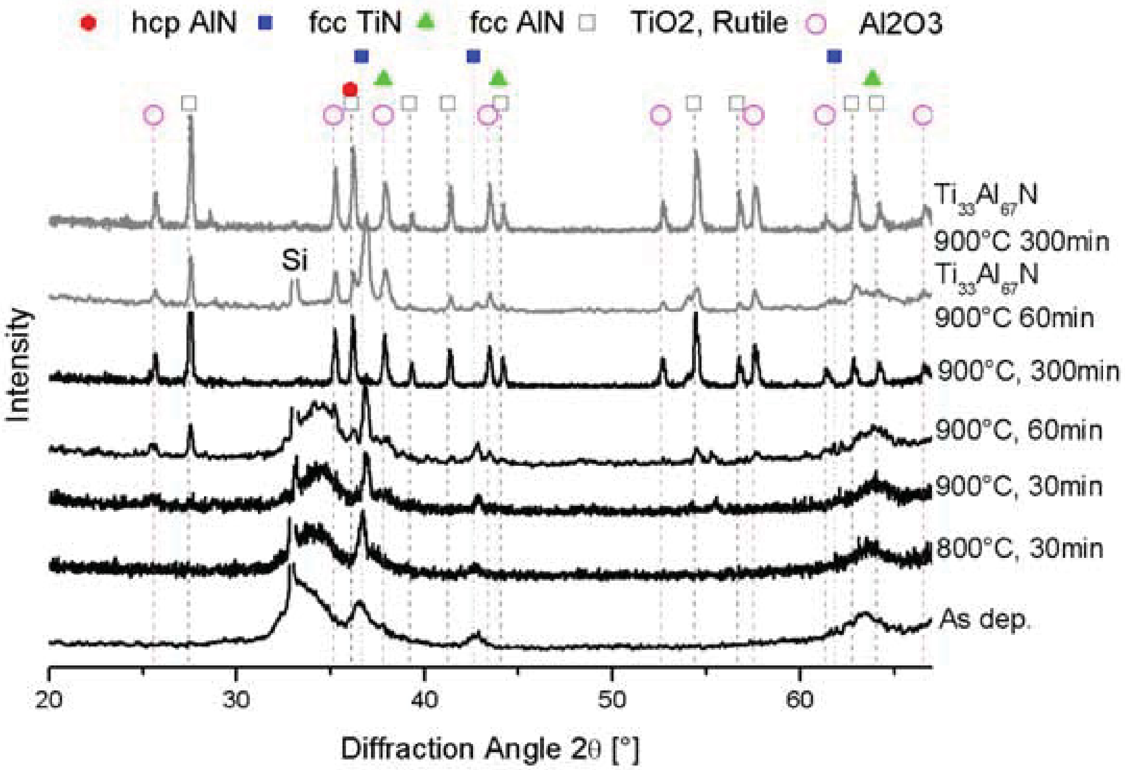

Fig. 4.6 XRD patterns for the different annealing states of $Ti_{32.5}Al_{67}B_{0.5}N$ on Si substrates, V_B= -40 V, compared to $Ti_{33}Al_{67}N$, V_B= -40 V annealed for 60 and 300 min at 900°C.

4.2 Raman Spectroscopy

4.2.1 Ti-Al-Si-N

As-deposited state

Fig. 4.7 shows representative Raman spectra of the $Ti_{33}Al_{67}N$ reference sample and the $Ti_{31}Al_{67}Si_2N$ coating. The coatings used for the measurement were deposited using a bias voltage of -40 V and were not annealed before testing. Standard Raman spectra are very limited and no spectra for fcc-TiN, fcc-AlN and hcp-AlN could be found. Thus, the identification of different nitride phases is not possible. However the spectra of the as-deposited coatings can be used to identify the onset of oxidation. Furthermore they can be used to distinguish between the nitride and oxide phases in the annealed samples, especially as the oxide bands tend to be rather sharp, which then can be easily distinguished from the curves recorded of the as-deposited samples.

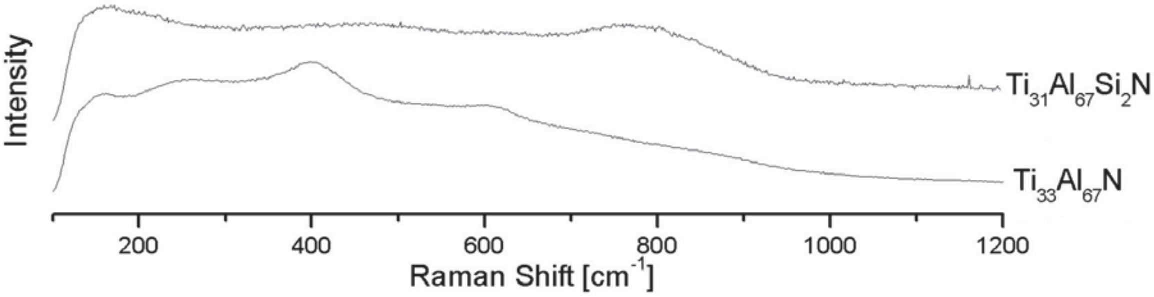

Fig. 4.7 Raman spectra of the as-deposited $Ti_{33}Al_{67}N$ and $Ti_{31}Al_{67}Si_2N$ coatings, both deposited at V_B= -40 V.

The oxidized state

The spectra obtained from the annealed samples were compared to the as-deposited curves as well as to standards of anatase, rutile and corundum. The peaks of the standard materials drawn in the following plots are taken from the RRUF Project website [81]. The assigned RRUF ID's are R060277.3, R040049.3 and R040096.3 for anatase, rutile and corundum, respectively.

The Raman spectra recorded of the as-deposited and oxidized $Ti_{31}Al_{67}Si_2N$ coatings are shown in Fig. 4.8. The spectrum of the specimen annealed at 800 °C shows no significant difference when compared to the as-deposited sample. The spectrum taken of the sample held for 30 min at 900 °C shows a strong peak at a wave number of 145 cm^{-1}. As can be seen in the plot, the peak indicates the formation of anatase, a TiO_2 modification. For longer annealing times additional anatase peaks appear, but even annealing the sample for 300 min does not show any signs of rutile formation. Comparing this result to the spectra taken of the pure $Ti_{33}Al_{67}N$ samples, one sees that both anatase and rutile have formed in the unalloyed sample, which was observed to be oxidized stronger according to the XRD measurements. None of the measured spectra show any signs of corundum peaks, which should appear at 379 cm^{-1} and 415 cm^{-1} and there are also no signs of other Al containing oxides found in the present spectra. Besides the intact samples, Raman spectroscopy allowed the measurment of some of the fractured -160 V biased samples, which could, due to their size, not be measured by XRD. The obtained spectra showed qualitatively the same results as obtained for the lower biased coatings.

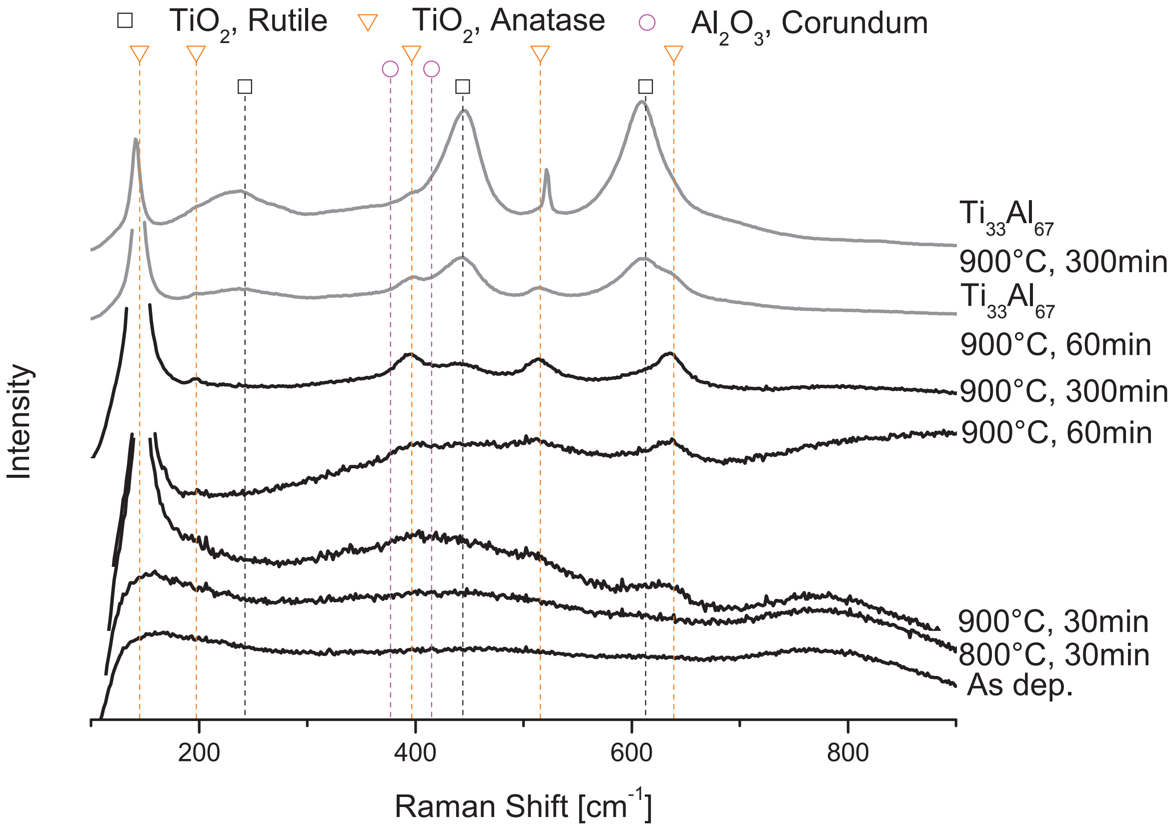

Fig. 4.8 Raman spectra of $Ti_{31}Al_{67}Si_2N$, V_B= -40 V annealed at the given parameters. Additionally the recorded spectra of $Ti_{33}Al_{67}N$, V_B= -40 V, annealed at 900 °C for 60 min and 300 min are plotted, respectively.

4.2.2 Ti-Al-B-N,

As-deposited state

Raman spectra recorded of the as-deposited $Ti_{32.5}Al_{67}B_{0.5}N$ and $Ti_{33}Al_{67}N$ coatings deposited at -40 V bias are shown in Fig. 4.9. Due to the lack of reference spectra, an identification of the nitride phases is not possible. This limits the use of the spectra to detect the onset of oxidation, characterized by the appearance of additional, mostly sharp bands of the formed oxide phases.

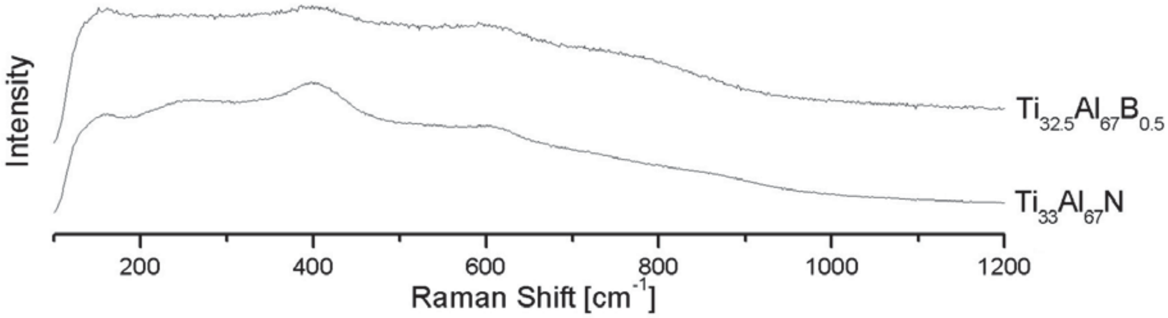

Fig. 4.9 Raman spectra of the as-deposited $Ti_{32.5}Al_{67}B_{0.5}N$ and $Ti_{33}Al_{67}N$ grown at -40 V bias.

The oxidized state

Fig. 4.10 shows the spectra taken of the $Ti_{32.5}Al_{67}B_{0.5}N$ coatings in the as-deposited and oxidized states. In addition the spectra of pure $Ti_{33}Al_{67}N$ held for 60 and 300min at 900 °C are plotted. The B alloyed coatings clearly exhibit anatase peaks at Raman shifts [cm^{-1}] of 145, 197, 397, 515, 639, indicating that oxidation has already started, when being annealed at 900 °C for 30 min. Increasing the holding time to 60 min at the same temperature leads to further anatase formation, but also to the appearance of a rutile peak at a wave number of 449 cm^{-1}. After annealing the coating for 300 min at 900 °C the anatase peaks diminished, only the peak at 145 cm^{-1} is still visible, while further rutile peaks appear in the spectrum. At these annealing parameters the B alloyed coatings appear to have qualitatevily a similar phase composition as the pure $Ti_{33}Al_{67}N$ reference sample. The behavior described here is found for all B and reference coatings and leads to the conclusion that during the early stages of oxidation anatase is formed, which transforms to the more stable rutile phase at higher temperatures or longer annealing times. As published in the paper of Orendorz et al. [82] and references therein, rutile appears to be the phase with the highest thermodynamic stability, which confirms the obtained results. In accordance with the Si alloyed and the unalloyed samples, no Al related peaks are found, despite, the XRD results indicate the presence of corundum in the oxide layer.

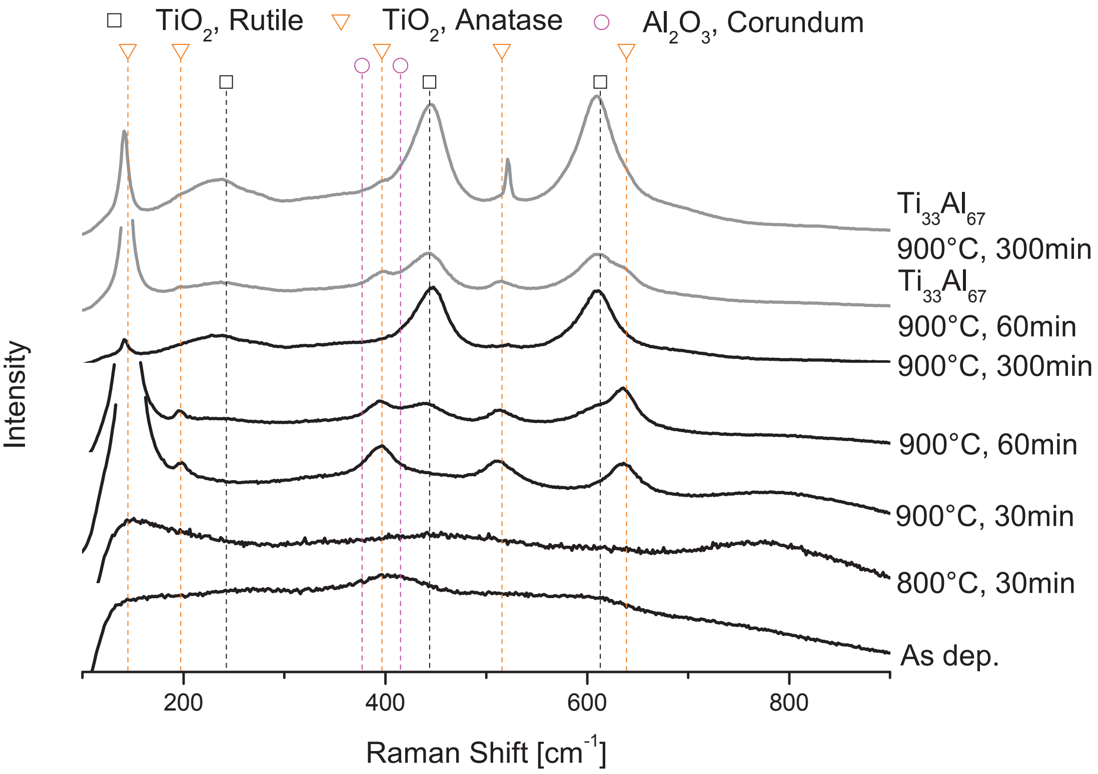

Fig. 4.10 Raman spectra of $Ti_{32.5}Al_{67}B_{0.5}N$, V_B= -40 V, annealed at the given parameters. Additionally the recorded spectra of $Ti_{33}Al_{67}N$, V_B= -40V, annealed at 900 °C for 60 and 300 min, respectively, are plotted.

4.3 Scanning Electron Microscopy

4.3.1 Ti-Al-Si-N

Fig. 4.11a-f shows secondary electron (SE) images taken of the cross-sectional fracture surfaces of as-deposited and oxidized $Ti_{31}Al_{67}Si_2N$ samples. At the bottom of each picture the uppermost part of the Si substrate can be seen. Above it a brighter band, being a TiN interlayer deposited below the actual $Ti_{1-x}Al_xN$-type coating is visible. The scale, found on top of the coating, is the oxide layer, whose thickness was measured. Starting with the as-deposited coating in Fig. 4.11a one can see an increase in oxide layer thickness when going to higher annealing temperatures and times. The maximum is observed in Fig. 4.11f, where the cross-section of the coating oxidized for 300 min at 900 °C is shown.

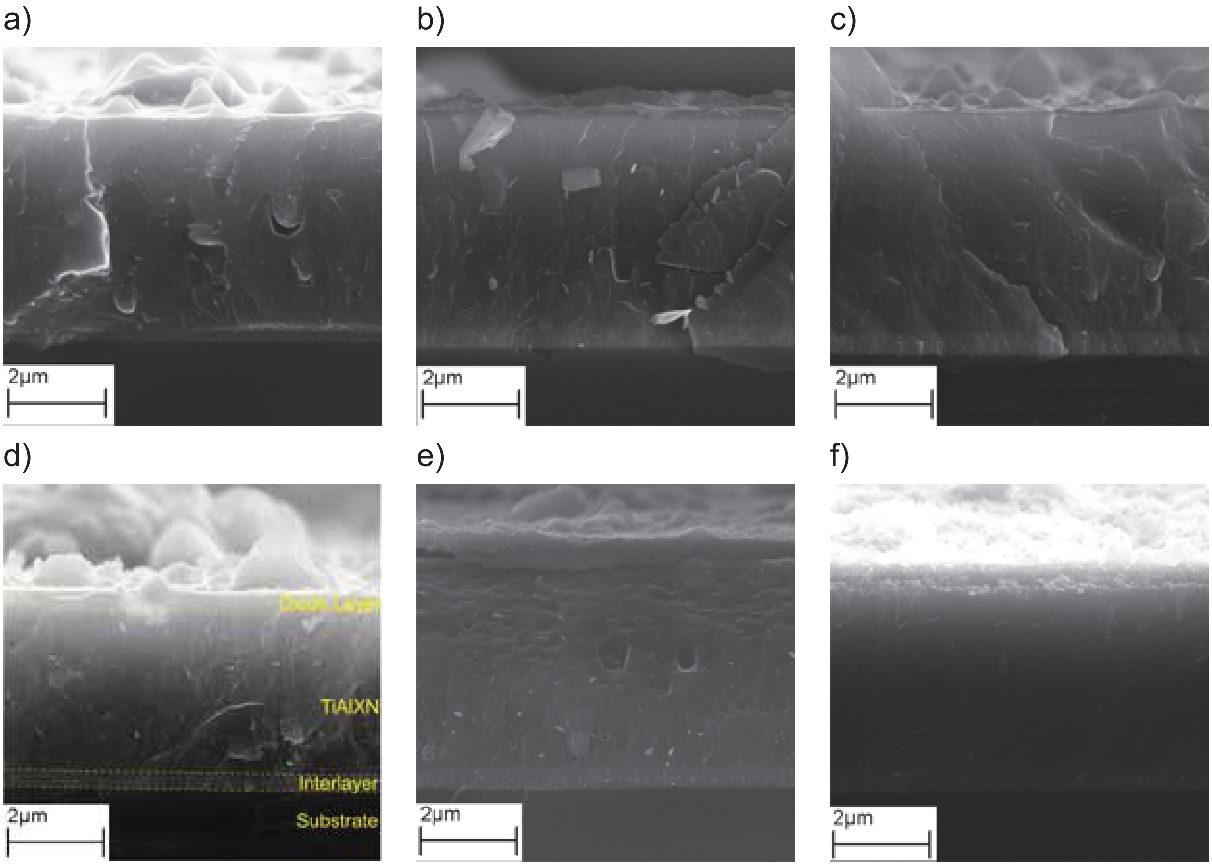

Fig. 4.11 Cross-sectional fracture surfaces of the $Ti_{31}Al_{67}Si_2N$ coatings, which underwent the following annealing procedures: (a) as-deposited; (b) 700 °C, 30 min; (c) 800 °C, 30 min; (d) 900 °C, 30 min; (e) 900 °C, 60 min; (f) 900 °C 300 min;

Plots of the oxide layer thickness versus the annealing conditions for the Si alloyed coatings are shown in Fig. 4.12. Fig. 4.12a and Fig. 4.12b show the results of the coatings deposited at -40 V and -160 V bias.

An average oxide layer thickness of about 700 nm is measured for the reference material after annealing for 30 min at 900 °C, while values of 348 and 319 nm are obtained for the coatings with 0.5 and 2 at.% Si content, respectively. Only slight oxide growth is observed for the alloyed coatings when doubling the annealing time. For both samples an almost equal scale thickness is found, while at the same time the layer of the unalloyed sample has grown to a thickness of more than 1.3 µm. The coating alloyed with 2 at.% Si exhibits the best oxidation resistance after being annealed for 300 min, as the layer thickness is only ~540 nm, compared to ~950 nm for the coating with lower Si content. The pure $Ti_{33}Al_{67}N$ coating is completely oxidized after this holding time, with no remaining nitride coating visible.

A higher applied V_B leads to an increase of the compressive residual stresses in the coatings, as reported by Pfeiler et al. in [36]. Due to differences in the coefficient of thermal expansion between Si substrate and coating, these compressive stresses are further increased, when the sample is heated up. Together with those superposed thermal stresses, this might explain why many of the coatings deposited at V_B= -160 V fractured or spalled of during annealing. Thus, it was impossible to determine the oxide layer thickness for some samples, leading to an incomplete diagram in Fig. 4.12b. For 2 at.% Si only the sample oxidized for 30 min at 900 °C survived annealing, with a measured oxide layer thickness of 460 nm. This is about 130 nm more than for the -40 V biased sample. Comparing the results for the different bias voltages of the coatings alloyed with 0.5 at.% Si, again the -160 V coatings show higher values of the oxide scale thickness at all temperatures. Unalloyed $Ti_{33}Al_{67}N$ exhibits a slightly higher oxide layer thickness, after oxidation at 800 °C and a dwell time of 30 min, than the alloyed sample. The reference sample annealed for 300 min at 900 °C was completely oxidized like at -40 V.

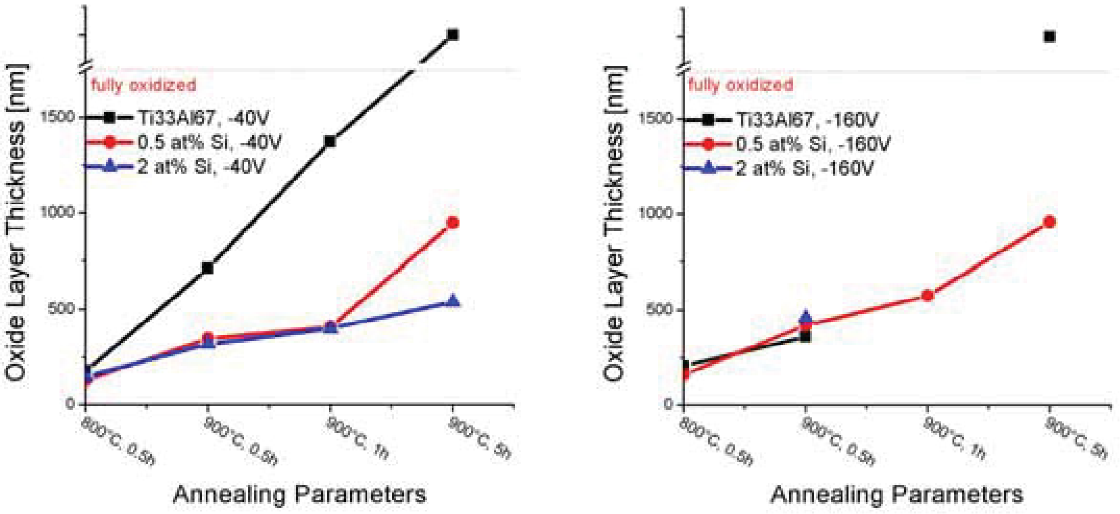

a) b)

Fig. 4.12 Oxide layer thickness versus annealing parameters for the Si alloyed coatings plotted separately for (a) V_B= -40 V and (b) V_B= -160 V.

4.3.2 Ti-Al-B-N

Fig. 4.13 shows a sequence of SEM pictures taken of the cross-sectional fracture surfaces of the B alloyed coating system $Ti_{32.5}Al_{67}B_{0.5}N$, deposited with V_B= -40 V. Again the separately distinguishable zones of the micrographs, i.e. substrate, nitride coating and oxide layer can be seen. An increase of oxide layer thickness is measurable with increasing time and temperature. In Fig. 4.13f, severe oxidation of the coating can be seen. The 300 min annealing procedure at 900 °C led to a complete oxidation of the original coating, forming a highly porous oxide layer of about 5 µm thickness, without any visible remainders of the nitride coating.

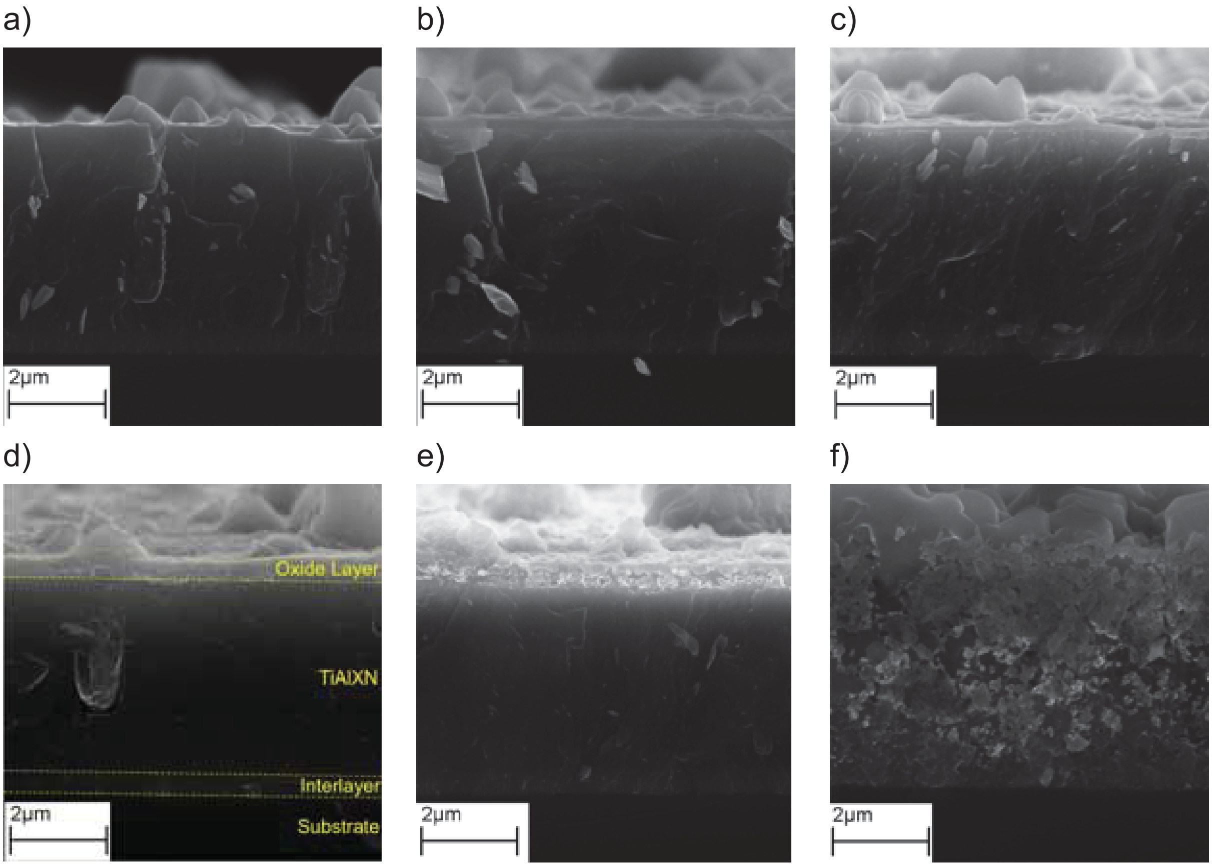

Fig. 4.13 SEM images of the coss-sectional fracture surfaces of the $Ti_{32.5}Al_{67}B_{0.5}N$ coatings deposited with V_B=-40 V and heat treated with the following temperatures and times: (a) as-deposited; (b) 700 °C, 30 min; (c) 800 °C, 30 min; (d) 900 °C, 30 min; (e) 900 °C, 60 min; (f) 900 °C 300 min;

The evaluation of the scale thickness measurements of the Ti-Al-B-N coatings is shown in the diagrams plotted in Fig. 4.14. In Fig. 4.14a, where the coatings deposited with V_B=-40 V are shown, the $Ti_{33}Al_{67}N$ reference sample has the thickest oxide layer at all examined annealing parameters, showing an improvement of the oxidation resistance by addition of B. Comparing the 0.1 at.% B and 0.5 at.% B coatings it can be seen that they exhibit nearly the same oxide layer thickness when annealed for 30 min at 900 °C. After 60 min of heat treatment at the same temperature, thicknesses of 850 nm and 630 nm are measured for the 0.1 and 0.5 at.% B coatings, respectively. All coatings are completely oxidized after the longest dwell time at 900 °C. The results indicate an increase in oxidation resistance with increasing B content.

Fig. 4.14b shows the results gained for the coatings deposited with V_B= -160 V. Due to the reasons described before the values of the reference sample are not complete. Nevertheless the data show the trend that oxidation resistance is better for the coating alloyed with 0.1 at.% B, compared to the one containing 0.5 at.% B, which exhibits a higher oxide layer thickness for both 900 °C, 30 min and 900 °C, 60 min. The limited results also indicate a decrease in oxidation resistance with increasing V_B, which is in good accordance with the results obtained for the Si alloyed coatings.

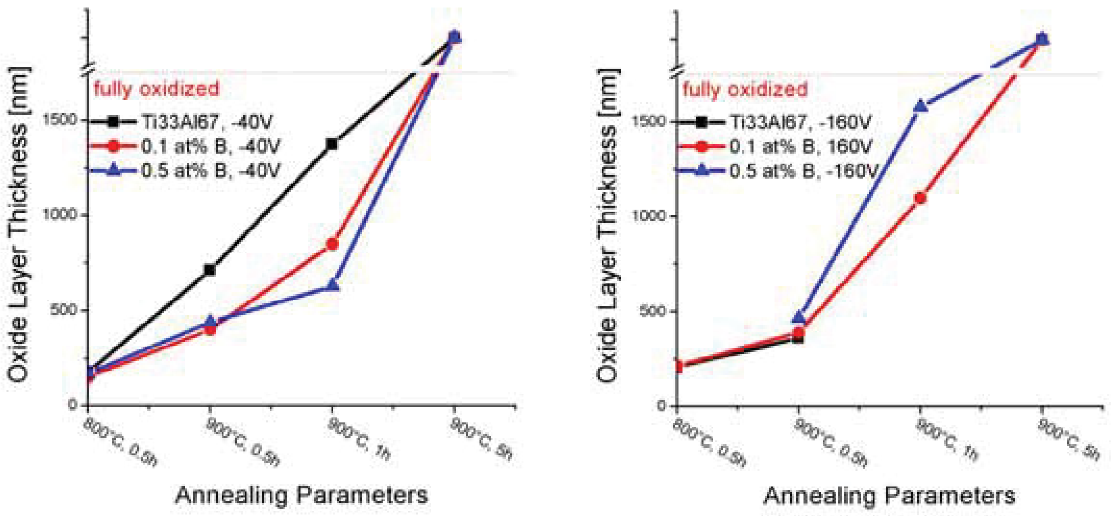

a) b)

Fig. 4.14 Oxide layer thickness plotted versus the annealing parameters for the Ti-Al-B-N coatings deposited with (a) V_B= -40 V, (b) V_B= -160 V.

4.4 EDX Linescan

In addition to the SE images an EDX linescan, which is a position sensitive EDX analysis conducted along a line perpendicular to the surface, was carried out in the SEM. The sample used was originally a $Ti_{31}Al_{67}Si_2N$ (V_B=-40 V) TEM specimen oxidized at 900 °C for 1h, which was not ion polished. It was chosen as a representative sample to prove or disprove the theory of sublayer formation in the oxide layer and to analyze the distribution of various elements within the oxide layer. The results of the linescan are shown in Fig. 4.15, where the oxide-adhesive interface was chosen as the origin of the abscissa, which points towards the Si substrate. The intensity plotted on the ordinate has to be read separately for every element and does not allow a quantitative comparison of the fractions of the different elements. The intensities given for the different elements, between 1 and 2.25 µm, correspond to those of the unoxidized nitride coating. Towards the specimen surface the N (red) content decreases, while a slight enrichment of Ti (green) is observed about 360 nm away from the surface, before the concentration also decreases when further approaching the surface. The Al (black) content first exhibits a minimum, at about the same x-value, where Ti shows the maximum, but afterwards increases again when getting closer to the oxide surface. The O (blue) concentration is high at the surface of the oxide scale, but afterwards decreases when getting closer to the nitride coating and presumably reaches very low levels inside the unoxidized coating. The content of the introduced Si (yellow) stays nearly constant throughout the measurement range, showing only a very small decrease near the oxide surface.

The results allow the assumption that Al diffuses to the surface forming an Al_2O_3 -sublayer with a respective Ti depleted zone. In the lower part of the oxide layer the opposite situation is encountered, with Ti enrichment, Al depletion, and the probable formation of TiO_2. This approves the theory of the separation of Ti and Al within the oxide scale and the formation of a two layered structure with the protective Al_2O_3 layer on the surface, which was proposed by McIntyre et al. in [52]. No apparent change, generated by oxidation, can be seen in the Si concentration. The slight decrease of the Si content visible at the surface of the specimen could be a result of the inaccuracy of the measurement, which is caused by the large volume from which the X-rays are emitted. The excited volume, being particularly large in structures with low density and lightweight elements, as described in [78], limits the resolution of the EDX linescan.

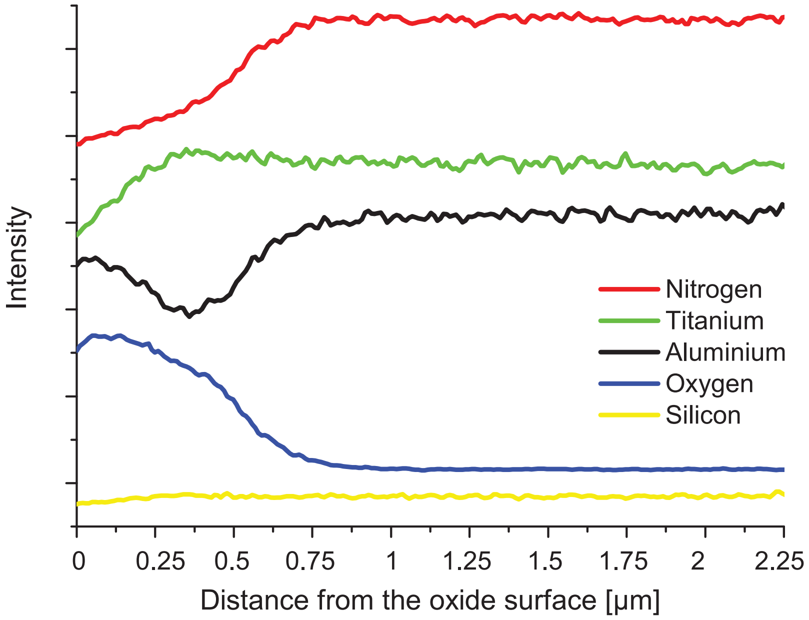

Fig. 4.15 The distribution of N, O, Al, Ti and Si in the oxide layer and the nitride coating, determined with the EDX linescan.

4.5 Transmission Electron Microscopy

4.5.1 Ti-Al-Si-N

As-deposited state

Fig. 4.16a shows a TEM image made of an as-deposited $Ti_{31}Al_{67}Si_2N$ coating deposited with a V_B of -40 V. The lowest visible part of the image shows the TiN interlayer, used to provide good adhesion, and adjacent to it the actual nitride coating in the upper part of the picture. The coating exhibits a dense structure and a preferred growth direction perpendicular to the substrate, which is not shown in the picture. SAED patterns were recorded of the substrate-coating interface and one is shown in Fig. 4.16b. It should be mentioned that the used aperture covers the whole area from the uppermost part of the substrate to the lowest part of the $Ti_{1-x}Al_xN$ coating. The black dot pattern results from the Si single crystal substrate, while the diffraction rings can be assigned to the different polycrystalline phases of the coating. Several of them lie between the rings of fcc-TiN and fcc-AlN and thus indicate the presence of a $Ti_{1-x}Al_xN$ solid solution in the coating. Additionally some rings in the pattern can be assigned to hcp-AlN, confirming the fcc-$Ti_{1-x}Al_xN$/hcp-AlN dual phase structure of the coatings, which was expected for the coatings deposited with V_B=-40 V. The pattern does not show signs of Si containing phases, allowing the assumption that the alloying content is in solid solution in the nitride phases.

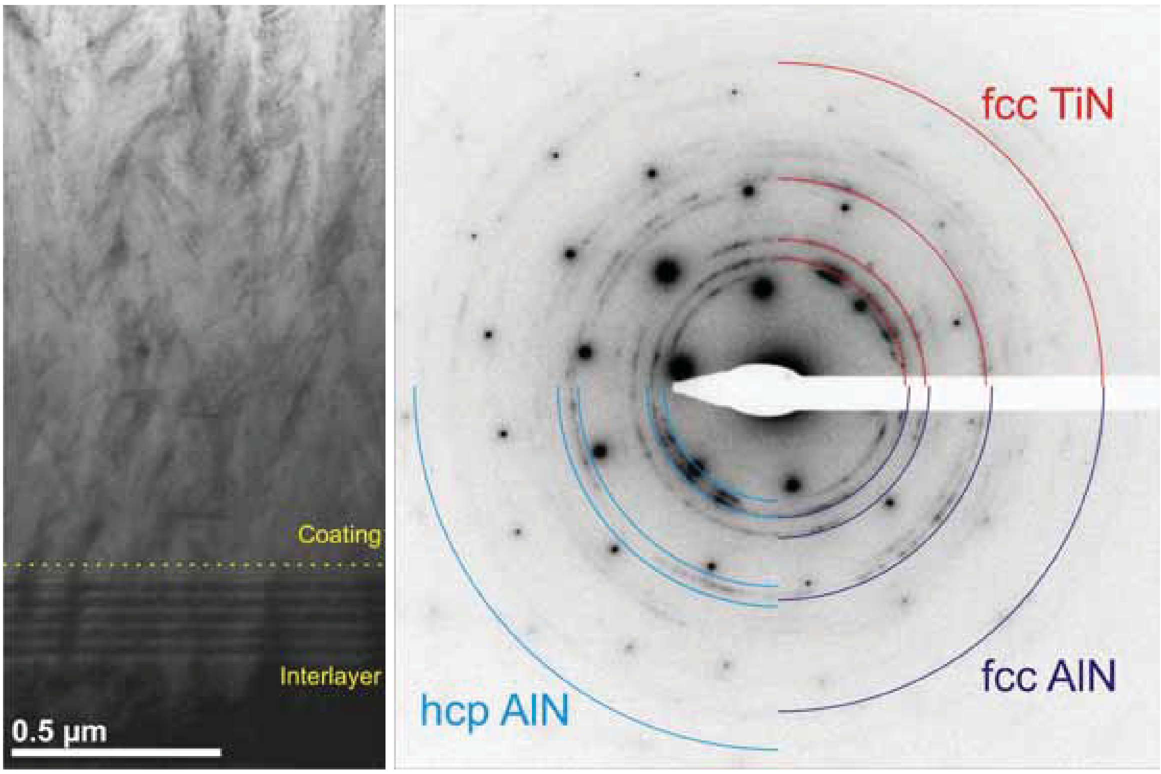

a) b)

Fig. 4.16 (a) TEM image of as-deposited $Ti_{31}Al_{67}Si_2N$, V_B=-40 V sample. (b) SAED image of the substrate-interlayer-coating area of the same sample.

The oxidized state

The oxide layer grown on a $Ti_{31}Al_{67}Si_2N$ (V_B=-40 V) coating, held for 60 min at 900°C, is shown in Fig. 4.17a. The lowermost part of the image shows the unoxidized coating, which has a structure similar to the as-deposited one. In the middle part of the picture the actual oxide layer can be seen, exhibiting a very porous structure and a high surface roughness. Remainders of the adhesive are visible in the uppermost part of the image.

An SAED pattern recorded in the middle of the oxide layer of the respective coating is shown in Fig. 4.17b. The absence of rings belonging to the nitride phases indicates the complete oxididation in this part of the original coating. The patterns found can be assigned to Al_2O_3, corundum and TiO_2 in the rutile modification. Furthermore patterns were recorded of the lower and near-surface parts of the oxide layer. They were similar to the one in Fig. 4.17b, showing both the presence of rutile and corundum. The conclusion drawn from these investigations is that no clear separation of rutile-rich and corundum-rich sublayers of the oxide layer can be detected by TEM. No rings indicating the presence of anatase were found in the SAED pattern taken of the near-surface region of the coating.

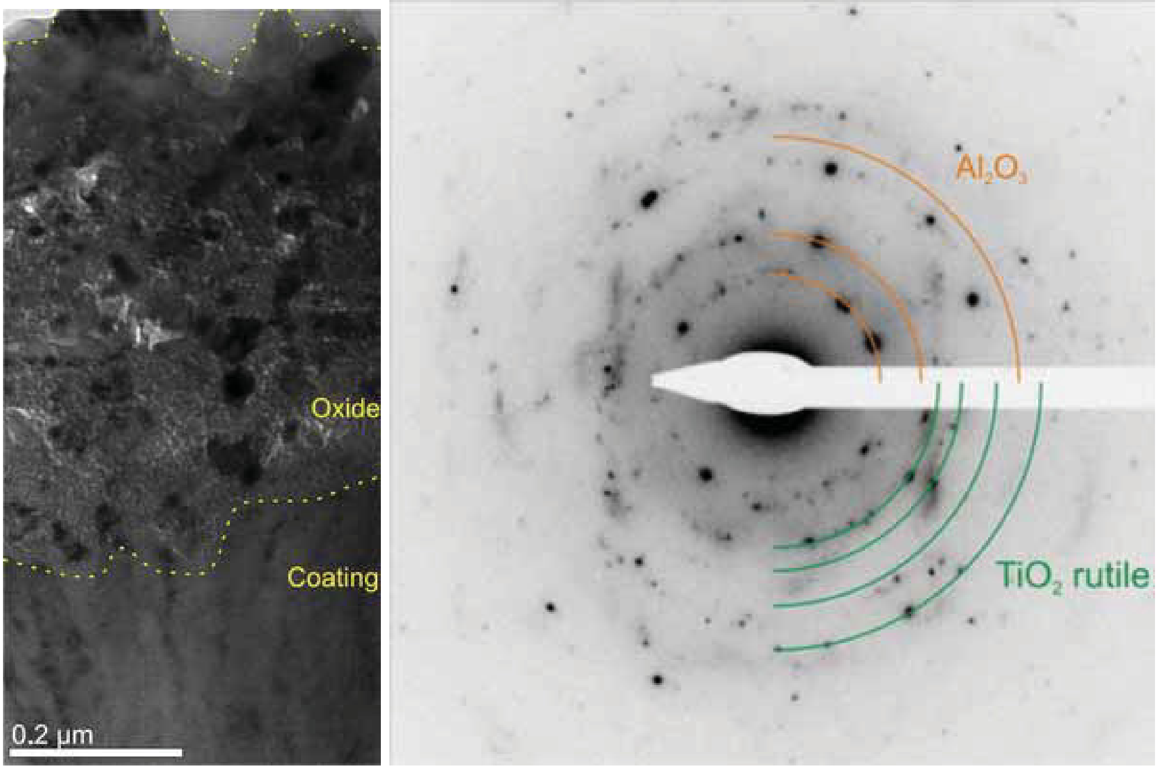

a) b)

Fig. 4.17 (a) TEM image of the $Ti_{31}Al_{67}Si_2N$ coating oxidized at 900 °C for 60 min. (b) Respective SAED image of the oxide layer.

4.5.2 Ti-Al-B-N

As-deposited state

An overview of the as-deposited $Ti_{32.5}Al_{67}B_{0.5}N$ (V_B=-40 V) coating is given in Fig. 4.18a. The lowermost section shows the Si substrate, with the interlayer adjacent to it. The upper part shows the B alloyed coating, exhibiting preferential growth towards the surface. Additionally a macroparticle, built into the coating, can be seen, which negatively affects the mechanical properties of the coating, as described in detail in [6]. Except the area below the droplet the coating exhibits a dense structure.

An SAED pattern of the coating-interlayer-substrate area is shown in Fig. 4.18b. Rings are found lying in between those of fcc-TiN and fcc-AlN, which indicates the existence of a $Ti_{1-x}Al_xN$ solid solution. As other diffraction rings could be assigned to hcp-AlN, the SAED shows that the as-deposited B alloyed coating consists of a dual phase fcc-$Ti_{1-x}Al_xN$/hcp-AlN structure.

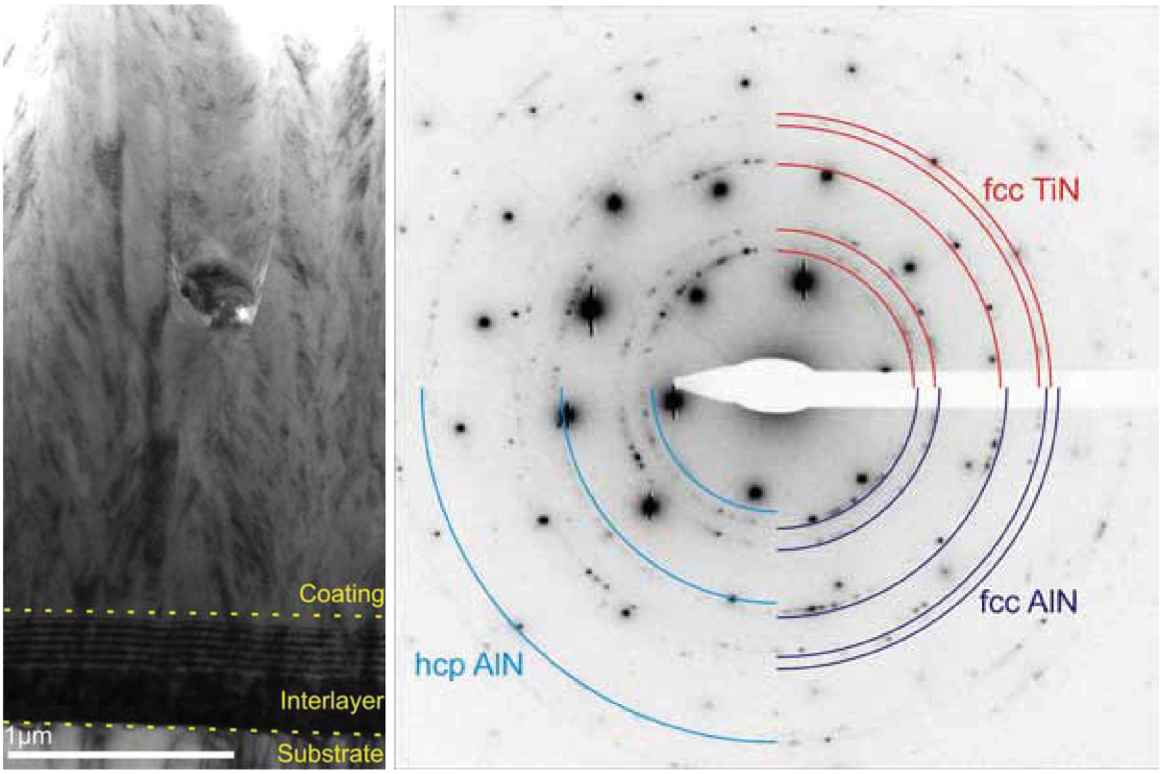

a) b)

Fig. 4.18 (a) A TEM image of $Ti_{32.5}Al_{67}B_{0.5}N$ in the as-deposited state. (b) SAED pattern taken from the substrate-interlayer-coating area of the respective coating.

The oxidized state

A TEM image made of a $Ti_{32.5}Al_{67}B_{0.5}N$ (V_B=-40 V) sample oxidized for 60 min at 900 °C is shown in Fig. 4.19a. It shows the unoxidized coating in the lower and the porous oxide layer in the middle part of the image. The topmost section of the picture shows a small band of remaining adhesive.

A SAED pattern recorded in the middle of the oxide layer (see Fig. 4.19b) revealed the presence of diffraction rings, which were assigned to TiO_2 in the rutile modification and Al_2O_3 in the corundum modification. No signs of remains of the original nitride coating were found, leading to the assumption that this part of the coating is oxidized. Also no evidence for the presence of anatase was found.

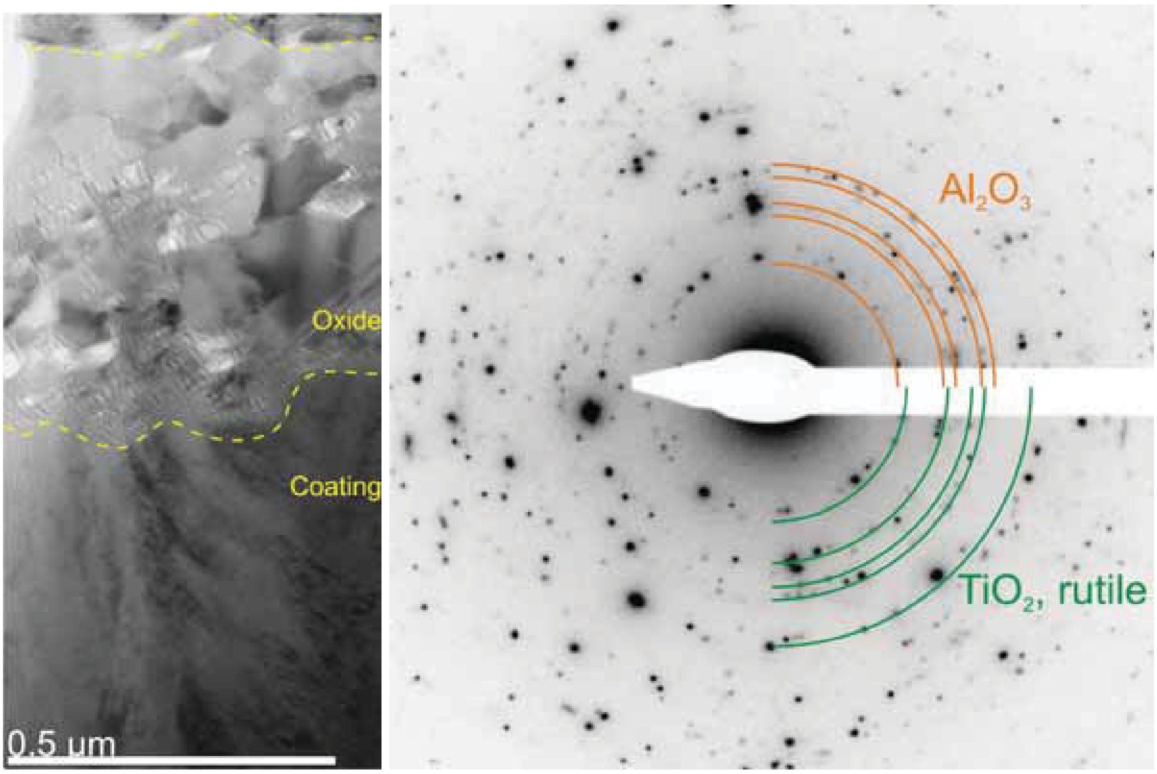

a) b)

Fig. 4.19 (a) TEM image of $Ti_{32.5}Al_{67}B_{0.5}N$ (V_B=-40 V) oxidized at 900 °C for 60 min. (b) Respective SAED image of the oxide layer.

5 Discussion

5.1 The As-deposited Coatings

The interpretation of the XRD and SAED patterns shows, that the $Ti_{33}Al_{67}N$ coatings deposited at -40 V bias exhibit a dual phase structure, consisting of fcc-$Ti_{1-x}Al_xN$ and hcp-AlN. This is in good accordance with the results reported by Kimura et al. [43], who observed the appearance of a dual phase zone between x-values of 0.6 and 0.7. The introduction of Si and B in the respective coating leads to more pronounced hcp-AlN peaks in the XRD patterns, which allows the assumption that both alloying elements promote the formation of the hcp-AlN phase at the expense of the fcc solid solution. This effect appears to increase with increasing alloying element content, which can be seen in the patterns of the -40 V biased coatings (see Fig. 4.1 and Fig. 4.4).

Raising V_B to -160 V suppresses the formation of the hcp-AlN phase, resulting in single phase fcc-$Ti_{1-x}Al_xN$ structures for the unalloyed and low-alloyed coatings, containing 0.5 at.% Si and 0.1 at.% B, respectively. Only the coatings alloyed with either 2 at.% Si or 0.5 at.% B still exhibit a dual phase fcc-$Ti_{1-x}Al_xN$/hcp-AlN structure, but with considerably lower fractions of the hcp phase, when compared to the lower biased coatings, as can be seen in Fig. 4.2 and Fig. 4.5.

Neither the XRD, nor the SAED patterns showed the presence of any Si or B related phases in the coatings. These results allow the assumption that the introduced elements are in solid solution and the contents are too low to form Si_3N_4 or BN. Vaz et al. [3] and Rebholz et al. [4] reported the presence of these phases in superhard coatings for higher alloying element contents of Si and B, respectively. On the other hand, the results are in good accordance with those published by Pilloud et al. [84] for Ti-Si-N with 0-4 at.% Si, who did not observe any phases besides TiN.

The TEM pictures taken of the as-deposited coatings gave an additional insight in the coating structure. They showed dense coatings with a preferred growth direction perpendicular to the surface and only few macroparticles.

5.2 The Oxidized Coatings

5.2.1 Oxide Layer Structure

The oxidized coatings were investigated by XRD, Raman spectroscopy and for, selected samples, also by TEM and SAED. The XRD patterns of the -40 V biased coatings and show the formation of the TiO_2 modification rutile and the Al_2O_3 modification corundum, at the onset of oxidation for all coatings. Rutile and corundum are generally reported as oxidation products of $Ti_{1-x}Al_xN$ coatings, as described by PalDey et al. in [30] and references therein. Both oxides are also found in the SAED patterns, confirming the XRD investigations. The first appearance of oxide peaks in the XRD patterns is observed at lower temperatures for the B alloyed coatings, than for the ones with introduced Si, indicating an earlier start of oxidation of the former. Furthermore, the XRD investigations reveal differences in the degree of oxidation for the coatings annealed for 300 min at 900 °C. While for the Si alloyed films, nitride peaks can still be observed, it appears that both of the B containing coatings did completely oxidize, with the XRD patterns showing only rutile and corundum peaks. An oxidation behavior similar to that of the B alloyed coatings is observed for the unalloyed $Ti_{33}Al_{67}N$ coatings, which allows the assumption that Si has an advantageous effect on the oxidation resistance of the $Ti_{1-x}Al_xN$ coatings. This behavior observed for the -40 V biased films is qualitatively also observed in the XRD patterns of the coatings deposited with V_B=-160 V.

Although Raman spectroscopy could not be successfully applied for the identification of nitride phases in the as-deposited coatings, due to the lack of reference patterns, the investigation of the oxidized coatings was used to identify the onset of oxidation and the oxidation products. The results for the onset of oxidation of the 0.5 at.% B alloyed coatings are in good accordance with the results obtained in the XRD measurements. In both cases the first oxide formation is observed after annealing the sample for 30 min at 900 °C. Contrary to the results of the XRD investigations, the first oxides are neither rutile nor corundum, but the TiO_2 modification anatase, which was not found at all in the XRD patterns. With increasing dwell time, rutile is increasingly detected at the expense of anatase, which is not unexpected, as rutile is the thermodynamically stable TiO_2 modification, as described by Orendorz et al. in [82].

Anatase formation is clearly observed for the specimen containing 2 at.% Si, which had been oxidized for 30 min at 900 °C. This suggests an earlier onset of oxidation than indicated by the XRD measurements, where the first signs of oxidation were found after twice the dwell time. Increasing the holding time seems to promote the anatase formation, but rutile could not be found even for the longest annealing times.

This somehow suprising finding could be related to a similar effect caused by Si in Ti-Si-N. Steyer et al. [85] found that the introduction of Si in TiN might favor the formation of TiO_2 in the modification anatase. In a recent paper Pilloud et al. [84] related this behavior to a grain size effect, which relates the phase stabilities of the different TiO_2 modifications to different grain size ranges. From the measurements conducted in this work no value of the anatase grain size can be derived, but nevertheless the grain size effect might be an explanation for the observed behavior. Despite the XRD and SAED results, no Al containing phases were detected with the Raman spectrometer.

McIntyre et al. [52] were the first ones reporting on the sublayered structure of the oxide scale forming on $Ti_{1-x}Al_xN$ coatings, consisting of an upper corundum-rich and a lower rutile-rich layer. To analyze the coatings used in this work with respect to this, an oxidized $Ti_{31}Al_{67}Si_2N$ sample was subjected to an EDX linescan. The results show an enrichment of Al in the surface-near part of the oxide layer, with a respective Ti depleted zone. In the coating-near part of the oxide scale, Al depletion and Ti enrichment were observed. These results, combined with the high O concentration throughout the scale, allow the assumption that a surface near corundum-rich and an underlying TiO_2-rich sublayer have formed. This approves the theory that a separation of the oxides occurs within the oxide layer. The EDX linescan does not allow an estimation on the degree of separation, but the SAED patterns show both corundum and rutile in all parts of the oxide scale, suggesting that the oxides did not fully separate into the sublayered structure. The nearly constant Si content throughout the oxide scale shows that the Si distribution is probably not affected by oxidation and diffusion processes connected with it.

5.2.2 Oxidation Resistance

In addition to the determination of the onset and qualitative degree of oxidation with XRD and Raman spectroscopy measurements, the evaluation of the oxide layer thicknesses measured in the SEM was used to gain a quantitative impression of the oxidation resistance of the various coatings.

Influence of B and Si

The SEM characterization of fracture cross-sections of the -40 V biased coatings (left half of Fig. 5.1) shows that the alloyed coatings possess an improved oxidation resistance with respect to the reference $Ti_{33}Al_{67}N$ coating. For both Si and B it is found, that increasing the content of the alloying element leads to higher oxidation resistance. A possible explanation of this behavior is that the introduced elements could impede the diffusion processes occuring during oxidation, or might modify the growth mechanisms and microstructure of the growing scale. The latter mechanisms are described in a general way in [24], whereas the former was found to be responsible for the improved oxidation behavior of TiN coatings doped with 5 at.% Si, by Diserens et al. [86]. The obtained oxide layer thicknesses of the Si alloyed coatings are thinner than those of the B alloyed ones, suggesting that Si improves oxidation resistance more effectively than B does, which implies, that not only the content, but also the type of alloying element is essential. A comparison of the curves for the coatings containing 0.5 at.% B and Si, respectively in Fig. 5.1, confirms this assumption as for all annealing conditions the Si doped coating is less oxidized.

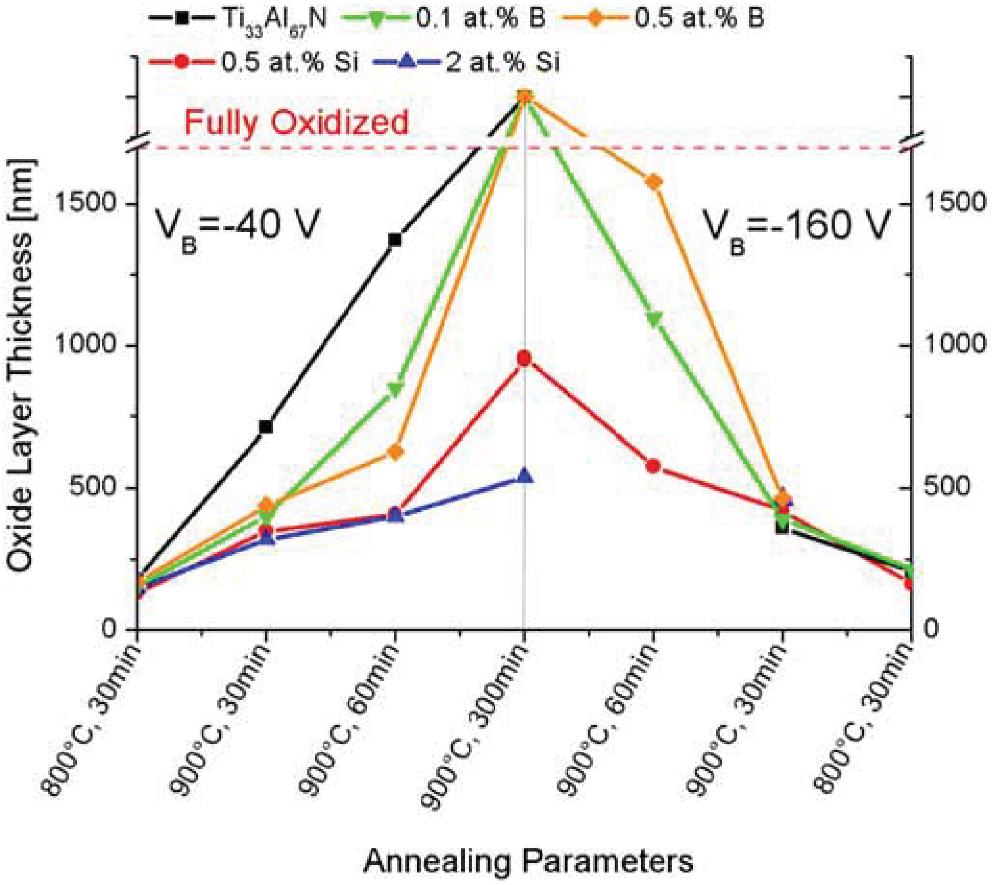

Fig. 5.1 Oxide layer thickness versus annealing parameters for the oxidized coatings with V_B=-40 V plotted in the left and V_B=-160 V plotted in the right half.

The influence of the chemical composition is very different for the coatings deposited at V_B=-160 V, which can be seen in the right half of Fig. 5.1. Due to residual and thermal stresses many of the samples broke into pieces or the coatings spalled of, hindering characterization in the SEM. The evaluation of the available data does not allow a complete comparison of the unalloyed and alloyed coatings, but shows that the influence of the alloying elements has changed. Contrary to the lower biased coatings, an increase of B and Si content has detrimental effects on the oxidation resistance, as these coatings exhibit more pronounced oxidation than the lower alloyed ones. This behavior can be linked to the phase composition of the coatings deposited with -160 V bias. The coatings containing 0.1 at.% and 0.5 at.% B and Si, respectively, crystallize in a solely fcc-$Ti_{1-x}Al_xN$ structure, whereas the higher alloyed ones still have a dual phase structure containing hcp-AlN. Vaz et al. [3] reported that the appearance of the wurtzite structure has detrimental effects on the oxidation resistance of $Ti_{1-x}Al_xN$, which would explain the behavior found for the -160 V biased coatings.

Influence of the Bias Voltage

Despite of the individual influences of the alloying elements a comparison of the left and right half of Fig. 5.1, showing the coatings deposited with -40 V and -160 V bias, respectively, reveals that V_B itself influences the oxidation behavior. The graph indicates that, independently of the chemical composition, the increased values of V_B deteriorate the oxidation resistance of the coatings. This behavior is unexpected as an increase of V_B should lead to a phase composition with less hcp-AlN, which was explained by Mayrhofer et al. in [39] and thus oxidation resistance should be improved. A positive influence of increasing ion energy was also reported by Mayrhofer et al. [83] for magnetron sputtered CrN coatings, who related this behavior to the introduced compressive stresses during coating growth.

A possible explanation for the behavior of the -160 V biased coatings could be related to an intensified generation of lattice defects, observed by Hakansson et al. [27] when applying high values of V_B. The diffusion coefficient is dependent on the defect and especially vacancy concentration of the material, which is described in detail in [87], and thus the higher V_B might be responsible for increased diffusion and the inferior oxidation resistance of the coatings. The sole exception to this behavior is the unalloyed reference material, where the oxide layer thickness decreases with increasing V_B, which could be an effect of the single phase fcc-$Ti_{1-x}Al_xN$ structure of the -160 V biased coating.

5.3 Comparison of XRD and Raman Spectroscopy

Concluding, a short comparison of XRD and Raman spectroscopy should be drawn, which were used to characterize the coatings. The conducted measurements exhibited both benefits and disadvantages of both methods. The better references available for the analysis of the XRD patterns allowed a complete identification of the nitride phases in the as-deposite state, which is currently not possible with Raman spectroscopy, due to the lack of nitride reference spectra. An additional, more fundamental problem arises from the fact that, due to selection rules explained in detail in [74], in Raman spectroscopy several excitational modes can not be displayed, which are then called forbidden or Raman inactive. According to Pilloud et al. [84] this applies to the first-order Raman spectra of perfect, defect free fcc-TiN. Therefore only defect-induced Raman spectra can be recorded of fcc-TiN, which are normally broad and of low intensity. Nevertheless at least hcp-AlN should be detectable by Raman spectroscopy, as reported by Bergman et al. in [88].

While XRD and SAED patterns reveal the presence of rutile and corundum in the oxidized state, Raman spectroscopy shows the formation of the TiO_2 modification anatase in the early stages of oxidation. This finding and the detection of the onset of oxidation are probably possible due to the high surface sensitivity reported for Raman spectroscopy in [75], allowing it to detect very thin oxide films. Nevertheless, also the Raman spectra give no complete overview of the oxidation products, as no signs of the Al incorporated in the coatings could be found, which is unexpected, as corundum is Raman active and exhibits a well-defined pattern, examined in [89] by Weber. If only a thin corundum layer forms on the oxide layer surface, as confirmed by the EDX linescan, it could be possible that the energy of the used laser, which was 100 mW, is sufficient to cause photochemical or thermal decomposition of the surface near corundum sublayer, which would explain the absence of corundum bands in the spectra. A practical advantage of Raman spectroscopy over XRD is the faster measurement procedure and the possibility to record patterns of small sample areas, which can be appointed by light microscopy. This made it possible to record patterns of small fragments of fractured samples, which could not be analyzed by XRD.

6 Summary and Conclusion

The aim of this thesis was to investigate the oxidation behavior of $Ti_{1-x}Al_xN$ coatings, alloyed with Si and B which were deposited by cathodic arc evaporation at different bias voltages. The introduction of Al into TiN hard coatings considerably improves the oxidation resistance, which made $Ti_{1-x}Al_xN$ a topic of intensive use and research during the past 20 years. A further improvement of the oxidation behavior was expected by the introduction of the alloying elements. The investigation of how they actually influence the coatings was the main goal of this thesis. The application of a bias voltage is known to have manifold influences on the structure, composition and the resulting properties of thin films. How these affect the oxidation behavior of the unalloyed and alloyed coatings was the second question posed.

$Ti_{33}Al_{67}$ was chosen as basic target composition, in which either 0.5 at.% Si, 2 at.% Si, 0.1 at.% B or 0.5 at.% B were introduced at the expense of the Ti content. Each of the different chemical compositions was deposited with two different bias voltages, being -40 V and -160 V, respectively, on Si wafer substrates. The deposition was carried out by Ceratizit Luxembourg on an Oerlikon-Balzers RCS system. Afterwards the coatings were oxidized in air at 700 °C, 800 °C and 900 °C, for 30 min each. Additionally the samples were held at 900 °C for 60 min and 300 min, to reach a more severe and pronounced oxidation of the coatings with high resistance to oxidation. The as-deposited and oxidized coatings were analyzed with XRD and Raman spectroscopy. This was conducted to determine their structure and occurring structural changes due to biasing and the oxidation treatment. SEM images were used to determine the oxide layer thickness after the different oxidation treatments, with the aim to obtain quantitative values for a direct comparison of the different coatings. TEM investigations of selected as-deposited and oxidized samples and an EDX linescan were conducted to gain a deeper insight in the structure of the oxide scale.

XRD measurements showed that all coatings deposited with V_B=-40 V exhibited a dual phase structure consisting of a fcc-$Ti_{1-x}Al_xN$ solid solution and hcp-AlN. The fraction of the hcp phase rose with increasing content of both Si and B, which allowed the assumption that both elements promoted the formation of the hcp-AlN phase. Increasing V_B to -160 V, lead to a suppression of the hcp-AlN phase. The unalloyed and lower alloyed coatings showed a single phase structure and only the coatings with 2 at.% Si and 0.5 at.% B still exhibited the dual phase structure.

The oxide layer was found to consist of TiO_2 rutile and Al_2O_3 corundum, when being analyzed by XRD. Raman spectroscopy additionally showed the formation of TiO_2

anatase in the oxide scale, in the early sages of oxidation, which partially transferred into rutile with increasing temperature and dwelling time. It was not possible to detect any corundum by Raman spectroscopy. Neither of the two measurement methods did show signs of the formation of Si or B containing phases in the coatings. Most likely, the Si and B contents are too low and the elements are in solid solution, or these phases are beyond the limit of detection. Overall, XRD measurements appear to give more comprehensive information than Raman spectroscopy does. Nevertheless the good surface sensitivity and the fast and easy measurement process make Raman spectroscopy a helpful additional measurement method.

The results of the SEM investigations showed, that the introduction of both Si and B improved the oxidation resistance of $Ti_{1-x}Al_xN$ coatings, when comparing them to unalloyed samples. The advantageous effect was found to be stronger for Si than for B. For the coatings deposited with V_B=-40 V, an increase of the alloying element content improved the oxidation resistance, while contrary to that in the V_B=-160 V biased coatings an increased content deteriorated the oxidation resistance. This behavior is explained by the effect, that both Si and B promoted the hcp-AlN formation, which is reported to have lesser oxidation resistance than the fcc phase. Of all tested coatings the one containing 2 at.% Si deposited at -40 V bias exhibited the best oxidation resistance. A comparison of the coatings with the same chemical composition, but deposited with different values of V_B, pointed out a deterioration of the oxidation resistance with increasing V_B. This was attributed to the increasing amount of defects generated by the higher V_B, which pose diffusion paths and may lead to increased oxidation.

The EDX linescan conducted on the $Ti_{31}Al_{67}Si_2N$, V_B=-40 V, sample, oxidized at 900 °C for 60 min, indicated a two-layered structure of the oxide scale. Near the surface, high fractions of Al and O were detected, while the underlying part showed an enrichment of Ti. Taking the results of the SAED pattern of this coating into account, it can be conducted that the oxide consists of a corundum-type top layer, with an underlying rutile-rich layer. In the linescan it was found that the Si content stayed nearly constant over the full oxide scale thickness, which indicated that the oxidation process had no influence on the Si distribution. The already mentioned SAED patterns recorded showed the presence of both corundum and rutile throughout the oxide layer, which allowed the assumption that the respective oxides had not completely separated during oxidation. Additional SAED patterns recorded of the nitride coatings showed a fcc-$Ti_{1-x}Al_xN$/hcp-AlN dual phase structure of the coatings deposited at -40 V bias. This confirms the results obtained in the XRD measurements, for both the oxide layer and the as-deposited coatings. TEM images showed a dense structure, with expected preferential growth direction, for both the Si and B containing coatings.

Finally it can be concluded, that alloying of $Ti_{33}Al_{67}N$ coatings with Si and B leads to an improvement of the oxidation behavior. The Si alloyed coatings generally tend to be better than the B alloyed ones, independently of the used V_B. Taking into account only the oxidation behavior of the coatings, lower values of V_B lead to better coating performance.

References

1. Fr.-W. Bach, A. Laarmann, T. Wenz, Modern Surface Technology, Wiley-VCH, Weinheim, 2006.

2. K. W. Mertz, H. A. Jehn, Praxishandbuch moderne Beschichtungen, Fachbuchverlag Leipzig, Leipzig, 2001.

3. F. Vaz, L. Rebouta, M. Andritschky, M.F. Da Silva, J.C. Soares, Surf. Coat. Technol. 98 (1998) 912-917.

4. C. Rebholz, A. Leyland, A. Matthews, Thin Solid Films 343-344 (1999) 242-245.

5. R.F. Bunshah, Handbook of Hard Coatings, Noyes Publications, Park Ridge, New Jersey, 2001.

6. J. L. Vossen, Werner Kern, Thin Film Processes II, Academic Press, San Diego, California, 1991.

7. D.M. Sanders, A. Anders, Surf. Coat. Technol. 133-134 (2000) 78-90.

8. M. Ohring, Materials Science of Thin Films, Academic Press, San Diego, California, 2002.

9. B. Jüttner, in Plasma Science, IEEE Transactions on, Vol. PS-15, No.5, Eindhoven, Netherlands, 1987, 474-480.

10. Fr.-W. Bach, T. Duda, Moderne Beschichtungsverfahren, Wiley-VCH, Weinheim, 2000.

11. B. Rother, J. Vetter, Plasma-Beschichtungsverfahren und Hartstoffschichten, Dt. Verlag für die Grundstoffindustrie, Leipzig, 1992.

12. D.A. Karpov, Surf. Coat. Technol. 96 (1997) 22-33.

13. D.L. Smith, Thin Film Deposition - Principles and Practice, Mc Graw Hill, New York, 1995.

14. S.G. Harris, E.D. Doyle, Y.-C. Wong, P.R. Munroe, J.M. Cairney, J.M. Long, Surf. Coat. Technol. 183 (2004) 283–294.

15. B.H. Hahn, J.H. Jun, in Plasma Surface Engineering, Vol. 2, (ed. E. Broszeit, W.D. Münz, H. Öchsner, K.-T. Rie, G. K. Wolf), DGM Informationsgesellschaft mbH, Oberusel, Germany, 1989, 1243-1250.

16. P.H. Mayrhofer, C. Mitterer, L. Hultman, H. Clemens, Prog. Mater. Sci. 51/8 (2006) 1032-1114.

17. J.E. Greene, in Handbook of Crystal Growth, Vol.1, (ed. D.T.J. Hurle), Elsevier, Amsterdam, Netherlands, 1993, 640-681.

18. I. Petrov, P.B. Barna, L. Hultman, J.E. Greene, J. Vac. Sci. Technol. A21 (5) (2003) 117-128.

19. J.A. Thornton, J. Ann. Rev. Mat. Sci. 7 (1977) 239-260.

20. P.B. Barna, M. Adamik, Thin Solid Films 317 (1998) 27-33.

21. R.D. Bland, G.J. Kominiak, D.M. Mattox, J. Vac. Sci. Technol. 11(4) (1974) 671-674.

22. R. Messier, A.P. Giri, R.A. Roy, J. Vac. Sci. Tech. A 2 (2) (1984) 500-503.

23. P.W. Atkins, J.A. Beran, General Chemistry, Scientific American Books, New York, 1992.

24. A.S. Khanna, Introduction to High Temperature Oxidation and Corrosion, ASM International, Materials Park, Ohio, 2002.

25. D.A. Jones, Principles and Prevention of Corrosion, Prentice Hall, Upper Saddle River, New Jersey, 1996.

26. N. Birks, G.H. Meier, Introduction to High Temperature Oxidation of Metals, Edward Arnold, London, 1983.

27. G. Hakansson, J.-E. Sundgren, D. McIntyre, J.E. Greene, W.-D. Münz, Thin Solid Films 153 (1987) 55-65.

28. A. Cavaleiro, B. Trindade, M.T. Vieira, in Nanostructured Coatings, (ed. A. Cavaleiro, J.T.M. DeHosson), Springer, New York, 2006, 261-314.

29. S.-Y. Yoon, K. O Lee, S.S. Kang, K.H. Kim, J. Mat. Proc. Tech. 130-131 (2002) 260-265.

30. S. PalDey, S.C. Deevi, Mater. Sci. Eng. A342 (2003) 58-79.

31. J.C. Schuster, J. Bauer, J. Solid State Chem. 53 (1984) 260-265.

32. H. Holleck, Surf. Coat. Technol. 36 (1988) 151-159.

33. K. Sato, N. Ichimiya, A. Kondo, Y. Tanaka, Surf. Coat. Technol. 163-164 (2003) 135-143.

34. K. Kutschej, P.H. Mayrhofer, M. Kathrein, P. Polcik, R. Tessadri, C. Mitterer, Surf. Coat. Technol. 200 (2005) 2358-2356.

35. H. Ljungcrantz, L. Hultman, J.-E. Sundgren, J. Appl. Phys. 78 (1995) 832-837.

36. M. Pfeiler, K. Kutschej, M. Penoy, C. Michotte, C. Mitterer, M. Kathrein, Surf. Coat. Technol. 202 (2007) 1050-1054.

37. M. Oden, J. Almer, G. Hakansson, Surf. Coat. Technol. 120–121 (1999) 272-276.

38. C.-S. Shin, D. Gall, N. Hellgren, J. Patscheider, I. Petrov, J.E. Greene, J. Appl. Phys. 93 (2003) 9086-9094.

39. P.H. Mayrhofer, D. Music, J.M. Schneider, J. Appl. Phys. 100 (2006) 1-5.

40. A.C. Vlasveld, S.G. Harris, E.D. Doyle, D.B Lewis, W.D. Münz, Surf. Coat. Technol. 149 (2002) 217–224.

41. O. Knotek, M. Böhmer, T. Leyendecker, J. Vac. Sci. Technol A4(6) (1986) 2695-2700.

42. R. Cremer, M. Witthaut, D. Neuschütz, in Value-Addition Metallurgy (ed. W.D. Cho, H.Y. Sohn), The Minerals, Metals & Materials Society, Warrendale, 1998, 249-258.

43. A. Kimura, H. Hasegawa, K. Yamada, T. Suzuki, Surf. Coat. Technol. 120-121 (1999) 438-441.

44. A.E. Santana, A. Karimi, V.H. Derflinger, A. Schütze, Thin Solid Films 469-470 (2004) 399-344.

45. A.N. Kale, D. Ravindranath, D.C. Kothari, P.M. Raole, Surf. Coat. Technol. 145 (2001) 60-70.

46. A. Hörling, L. Hultmann, M. Odén, J. Sjölén, L. Karlsson, Surf. Coat. Technol. 191 (2005) 384–392.

47. A. Hörling, L. Hultmann, M. Odén, J. Sjölén, L. Karlsson, J. Vac. Sci. Technol. A 20(5) (2002) 1815-1823.

48. P.H. Mayrhofer, A. Hörling, L. Karlsson, J. Sjölén, T. Larsson, C. Mitterer, L. Hultman, Appl. Phys. Lett. 83(10) (2003) 2049-2051.

49. L. Hultman, Vacuum 57 (2000) 1-30.

50. J.H. Hsieh, A.L.K. Tan, X.T. Zeng, Surf. Coat. Technol. 201 (2006) 4094-4098.

51. M. Wittmer, J. Noser, H. Melchior, J. Appl. Phys. 52(11) (1981) 6659-6664.

52. D. McIntyre, J.E. Greene, G. Hakansson, J.-E. Sundgren, W.-D. Münz, J. Appl. Phys. 67 (1990) 1542-1553.

53. F. Vaz, L. Rebouta, M. Andritschky, M. F. da Silva, J. C. Soares, J. Europ. Cer. Soc. 17 (1997) 1971-1977.

54. M. Kawate, A.K. Hashimoto, T. Suzuki, Surf. Coat. Technol. 165 (2003) 163-167.

55. S. Inoue, H. Uchida, Y. Yoshinaga, K. Koterazawa, Thin Solid Films 300 (1997) 171-176.

56. M. Zhou, Y. Makino, M. Nose, K. Nogi, Thin Solid Films 339 (1999) 203-208.

57. A. Joshi, H.S. Hu, Surf. Coat. Technol. 76-77 (1995) 499-507.

58. O. Knotek, M. Böhmer, T. Leyendecker, F. Jungblut, Mater. Sci. Eng. A105-106 (1988) 481-488.

59. H.W. Hugosson, H. Högberg, M. Algren, M. Rodmar, T.I. Selinder, J. Appl. Phys. 93(8) (2003) 4505-4511.

60. O. Knotek, W.-D. Münz, T. Leyendecker, J. Vac. Sci. Technol A5(4) (1987) 2173-2179.

61. L.A. Donohue, I.J. Smith, W.-D. Münz, I. Petrov, J.E. Greene, Surf. Coat. Technol. 94-95 (1997) 226-231.

62. M. Moser, P.H. Mayrhofer, Scripta Mater. 57 (2007) 357–360.

63. K. Kutschej, P.H. Mayrhofer, M. Kathrein, P. Polcik, C. Mitterer, Surf. Coat. Technol. 188–189 (2004) 358– 363.

64. A. Niederhofer, P. Nesládek, H.-D. Maennling, K. Moto, S. Veprěk, M. Jílek, Surf. Coat. Technol. 120–121 (1999) 173-178.

65. S. Carvalho, F. Vaz, L. Rebouta, D. Schneider, A. Cavaleiro, E. Alves, Surf. Coat. Technol. 142-144 (2001) 110-116.

66. S. Carvalho, E. Ribeiro, L. Rebouta, C. Tavares, J.P. Mendonca, A. Caetano Monteiro, N.J.M. Carvalho, J.T.M. DeHosson, A. Cavaleiro, Surf. Coat. Technol. 177 –178 (2004) 459–468.

67. K. Kutschej , N. Fateh, P.H. Mayrhofer , M. Kathrein , P. Polcik , C. Mitterer, Surf. Coat. Technol. 200 (2005) 113-117.

68. M. Baker, S. Klose, C.Rebholz, A. Leyland, A. Matthews, Surf. Coat. Technol. 151-152 (2002) 338-343.

69. C. Rebholz, A. Leyland, A. Matthew, C. Charitidis, S. Logothetidis, D. Schneider, Thin Solid Films 514 (2006) 81-86.

70. Balzer RCS Rapid Coating System, brochure taken from http://www.balzers.ch/bfl/ger/05-company/09-infomaterial/indexW3DnavidW269.php, May 5th 2008.

71. A.E. Santana, A. Karimi, V.H. Derflinger, A. Schütze, Surf. Coat. Technol. 177-178 (2004) 260-266.

72. R.L. Snyder, in X-ray Characterization of Materials, (ed. E. Lifshin), Wiley VCH, Weinheim, Germany, 1999.

73. M. Birkholz, Thin Film Analysis by X-Ray Scattering, Wiley VCH, Weinheim, Germany, 2006.

74. R. Merlin, A. Pinczuk, W.H. Weber, in Raman Scattering in Materials Science, (ed. W.H. Weber, R. Merlin), Springer, Heidelberg, Germany, 2000, 1-34.

75. L. Nasdala, D.C. Smith, R. Kaindl, M.A. Ziemann, in EMU Notes in Mineralogy 6, (ed. A. Beran, E. Libowitzky), European Mineralogical Union, Vienna, 2004.

76. Chair of Mineralogy and Petrology, at the University of Leoben, Austria, http://institute.unileoben.ac.at/mineralogie/Geraete.html#Analytical_Instruments, May 3rd 2008.

77. J.P. Eberhart, Structural and Chemical Analysis of Materials, Wiley VCH, Weinheim, Germany, 1991.

78. D.C. Joy, in Electron Microscopy - Principles and Fundamentals, (ed. S. Amelinckx, D. van Dyck, J. van Landuyt, G. van Tendeloo), Wiley VCH, Weinheim, Germany, 1997.

79. K.E. Sickafus, in Encyclopedia of Materials Characterization, (ed. C.R. Brundle, C.A. Evans Jr., S. Wilson), Butterworth-Heinemann, Stoneham, Massachusetts, 1992.

80. Department of Material Physics, at the University of Leoben, Austria, http://www.oeaw.ac.at/esi/english/research/facilities/em/tem.html, May 4th 2008.

81. RRUF^{TM} Project, http://rruff.info/, 23.04.2008.

82. A. Orendorz, A. Brodyanski, J. Lösch, L.H. Bai, Z.H. Chen, Y.K. Le, C. Ziegler, H. Gnaser, Surface Science 600 (2006) 4347-4351.

83. P.H. Mayrhofer, H. Willmann, C. Mitterer, Surf. Coat. Technol. 146 –147 (2001) 222–228.

84. D. Pilloud, J.F. Pierson, M.C. Marco de Lucas, A. Cavaleiro, Surf. Coat. Technol. 202 (2008) 2413-2417.

85. P. Steyer, D. Pilloud, J.F. Pierson, J.-P. Millet, M. Charnay, B. Stauder, P. Jacquot, Surf. Coat. Technol. 201 (2006) 4158-4162.

86. M. Diserens, J. Patscheider, F. Levy, Surf. Coat. Technol. 120-121 (1999) 158-165.

87. P. Haasen, Physical Metallurgy, Cambridge Univeristy Press, Cambridge, Great Britain, 1996.

88. L. Bergman, M. Duttra, R.J. Nemanich, in Raman Scattering in Materials Science, (ed. W.H. Weber, R. Merlin), Springer, Heidelberg, Germany, 2000, 273-313.

89. W.H. Weber, in Raman Scattering in Materials Science, (ed. W.H. Weber, R. Merlin), Springer, Heidelberg, Germany, 2000, 233-270.